

AD-A099 616

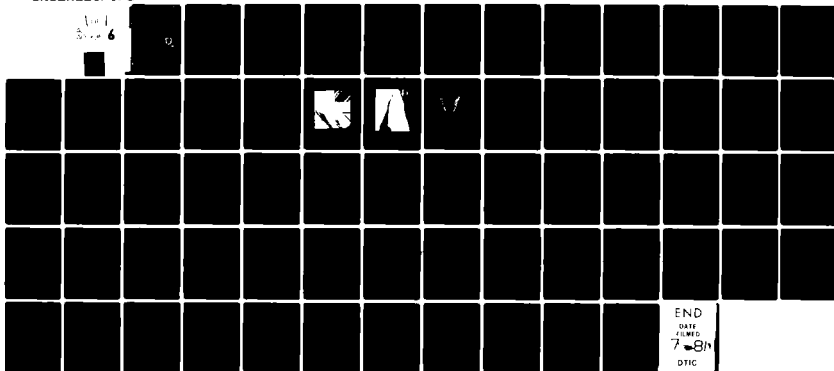
TEXAS UNIV AT AUSTIN DEPT OF AEROSPACE ENGINEERING AN--ETC F/6 20/4
THE TRANSONIC FLOW FIELD FOR A FLUIDIC-GENERATOR FUZE ASSEMBLY. (U)
MAY 81 J J BERTIN, T E HAYDEN, R L GOODYEAR DAAK21-80-P-5171

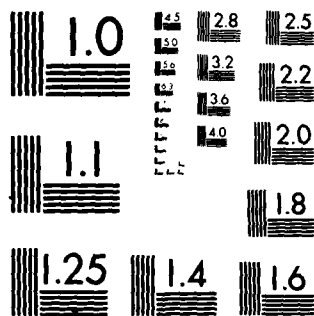
UNCLASSIFIED

HDL-CR-81-171-1

NL

1-1
6





MICROCOPY RESOLUTION TEST CHART
NATIONAL BUREAU OF STANDARDS-1963-A

AD A 099 676

HDL CR-81-171-1

MAY 81

LEVEL II

12 62

12

The Transonic Flow Field for a Fluidic-Generator Fuze Assembly,

by John J. Bertin Timothy E. Hayden Richard L. Goodyear

9 Contractor rept.,

Prepared by

University of Texas at Austin
Austin, TX 78712

Under purchase order

15 DAAK21-80-P-5171

DTIC
ELECTE
JUN 2 1981
S D E



U.S. Army Electronics Research
and Development Command
Harry Diamond Laboratories
Adelphi, MD 20783

Approved for public release; distribution unlimited.

DTIC FILE COPY

81 6 01 180

402465

The findings in this report are not to be construed as an official Department of the Army position unless so designated by other authorized documents.

Citation of manufacturers' or trade names does not constitute an official indorsement or approval of the use thereof.

Destroy this report when it is no longer needed. Do not return it to the originator.

UNCLASSIFIED

SECURITY CLASSIFICATION OF THIS PAGE (When Data Entered)

| REPORT DOCUMENTATION PAGE | | READ INSTRUCTIONS BEFORE COMPLETING FORM |
|--|---------------------------------------|--|
| 1. REPORT NUMBER HDL-CR-81-171-1 | 2. GOVT ACCESSION NO. ADA A099 616 | 3. RECIPIENT'S CATALOG NUMBER |
| 4. TITLE (and Subtitle) The Transonic Flow Field for a Fluidic-Generator Fuze Assembly | | 5. TYPE OF REPORT & PERIOD COVERED Contractor Report |
| | | 6. PERFORMING ORG. REPORT NUMBER |
| 7. AUTHOR(s) John J. Bertin and Timothy E. Hayden (University of Texas at Austin); Richard L. Goodyear (Harry Diamond Laboratories) | | 8. PURCHASE ORDER DAAK21-80-P-5171 <i>new</i> |
| 9. PERFORMING ORGANIZATION NAME AND ADDRESS Department of Aerospace Engineering and Engineering Mechanics UT Austin, Austin TX 78712 | | 10. PROGRAM ELEMENT, PROJECT, TASK AREA & WORK UNIT NUMBERS P69600R |
| 11. CONTROLLING OFFICE NAME AND ADDRESS Harry Diamond Laboratories 2800 Powder Mill Road Adelphi, MD 20783 | | 12. REPORT DATE May 1981 |
| | | 13. NUMBER OF PAGES 63 |
| 14. MONITORING AGENCY NAME & ADDRESS (if different from Controlling Office) | | 15. SECURITY CLASS. (of this report) UNCLASSIFIED |
| | | 15a. DECLASSIFICATION/DOWNGRADING SCHEDULE |
| 16. DISTRIBUTION STATEMENT (of this Report) Approved for public release; distribution unlimited. | | |
| 17. DISTRIBUTION STATEMENT (of the abstract entered in Block 20, if different from Report) | | |
| 18. SUPPLEMENTARY NOTES HDL Project No.: <u>4500D6</u> DRCMS Code: <u>69600R9050122</u> | | |
| 19. KEY WORDS (Continue on reverse side if necessary and identify by block number) Fluidic generator, rocket fuze, MLRS, nose-cone aerodynamics, rocket trajectory simulation, pressure measurements at rocket nose | | |
| 20. ABSTRACT (Continue on reverse side if necessary and identify by block number) An experimental program has been conducted to evaluate the performance of the fluidic-generator fuze assembly of the Army's Multi-Launch Rocket System (MLRS) in the transonic speed range. Static-pressure measurements and Pitot-pressure measurements were obtained for different nose configurations during a test program which was conducted in the Aerodynamic Wind Tunnel at the Arnold Engineering Development Center. The test conditions | | |

UNCLASSIFIED

SECURITY CLASSIFICATION OF THIS PAGE (When Data Entered)

UNCLASSIFIED

SECURITY CLASSIFICATION OF THIS PAGE(When Data Entered)

20. (cont'd)

included free-stream Mach numbers from 0.95 to 1.3 over a range of free-stream densities simulating altitudes from 15,240 m to 21,030 m. The pressure data from these tests have been analyzed to describe the internal and the external flow fields.

The pressures measured at the inlet hole for the fluidic-generator assembly is in close agreement with that given by the normal shock relations. The experimentally determined pressure ratio (p/p_{t2}) decreased as the free-stream Mach number increased for all external orifices from $x = 0.030 x_0$ to $1.000 x_0$. These Mach-number variations were gradual and consistent. Since flow through the fluidic-generator assembly is choked by the nozzle centerbody, the mass-flow rate can be correlated in terms of the external flow conditions.

p sub t2

if sub 0

| | |
|--------------------|-------------------------------------|
| Accession For | |
| NTIS GRA&I | <input checked="" type="checkbox"/> |
| DTIC TAB | <input type="checkbox"/> |
| Unannounced | <input type="checkbox"/> |
| Justification | |
| By | |
| Distribution/ | |
| Availability Codes | |
| Dist | Avail and/or Special |
| A | |

UNCLASSIFIED

SECURITY CLASSIFICATION OF THIS PAGE(When Data Entered)

CONTENTS

| | <u>Page</u> |
|--|-------------|
| 1. INTRODUCTION | 7 |
| 2. EXPERIMENTAL PROGRAM | 9 |
| 3. RESULTS | 15 |
| 3.1 External Pressures for 0° Angle of Attack . . | 15 |
| 3.1.1 Pressures on Flat Face ($x = 0.0$) | 15 |
| 3.1.2 Pressures on Conical Surface of Ogive | 21 |
| 3.2 Flow Through Fluidic Generator and Inter- nal Pressure Measurements for 0° Angle of Attack | 39 |
| 3.3 External and Internal Flow Fields for C2 at 0° Angle of Attack | 47 |
| 3.4 Effect of Angle of Attack | 51 |
| 4. CONCLUSIONS ABOUT FLOW FIELD | 55 |
| 4.1 External Flow Field | 55 |
| 4.2 Internal Flow Field | 57 |
| 4.3 Final Comments | 58 |
| NOMENCLATURE | 59 |
| LITERATURE CITED | 61 |
| DISTRIBUTION | 63 |

FIGURES

| | |
|--|----|
| 1 Army/MLRS fluidic-generator/fuze assembly | 10 |
| a External geometry | 10 |
| b Details of generator installation | 11 |
| c Details and installation of fuze ogive adapter (C2) | 11 |
| 2 Schlieren photographs from the tests of ref. 3 . . | 16 |
| a $M_\infty = 1.5$ | 16 |
| b $M_\infty = 5$ | 17 |

FIGURES (Cont'd)

| | <u>Page</u> |
|---|-------------|
| 3 Location of pressure sensors for C1, C4, and C9 and sketch of pressure distribution for a flat-faced cylinder (ref. 4) | 18 |
| 4 Pressure coefficients for flat face as a function of free-stream Mach number | 20 |
| 5 Flow models for (low) supersonic flow over standard nose cone | 22 |
| a Configuration 1 (C1) | 22 |
| b Configuration 4 (C4) | 22 |
| 6 Proposed flow model and relation between flow phenomena and instrumentation | 23 |
| 7 Comparison between theoretical and experi- mental pressure distribution, $M_\infty = 1.3$, AD = 18,290 m, $\alpha = 0^\circ$ | 24 |
| 8 Effect of density altitude (AD) on local static pressure for $M_\infty = 0.95$ | 27 |
| a $x = 0.213 x_0$ (tap 12) | 27 |
| b $x = 0.396 x_0$ (tap 23) | 27 |
| c $x = 0.551 x_0$ (tap 18) | 27 |
| 9 Effect of AD on local static pressure for $M_\infty = 1.13$ | 28 |
| a $x = 0.213 x_0$ (tap 12) | 28 |
| b $x = 0.396 x_0$ (tap 23) | 28 |
| c $x = 0.551 x_0$ (tap 18) | 28 |
| 10 Effect of AD on local static pressure for $M_\infty = 1.3$ | 29 |
| a $x = 0.213 x_0$ (tap 12) | 29 |
| b $x = 0.396 x_0$ (tap 23) | 29 |
| c $x = 0.551 x_0$ (tap 18) | 29 |

FIGURES (Cont'd)

| | <u>Page</u> |
|--|-------------|
| 11 Effect of inlet on pressure distributions for AD = 18,290 m | 31 |
| a $M_{\infty} = 0.95$ | 31 |
| b $M_{\infty} = 1.1$ | 31 |
| c $M_{\infty} = 1.2$ | 32 |
| d $M_{\infty} = 1.3$ | 32 |
| 12 Effect of Mach number on pressure dis- tributions for AD = 18,290 m | 34 |
| 13 Effect of Mach number on pressure dis- tributions for AD = 21,030 m | 35 |
| 14 Effect of Mach number on local pressures | 36 |
| a $x = 0.213 x_0$ (tap 12) | 36 |
| b $x = 0.396 x_0$ (tap 23) | 36 |
| c $x = 0.551 x_0$ (tap 18) | 37 |
| d $x = 1.000 x_0$ (tap 22) | 37 |
| 15 Internal flow pattern and relevant pressure information | 40 |
| 16 Static pressure distributions on internal surface of C1 | 41 |
| a AD = 18,290 m | 41 |
| b AD = 19,200 m | 41 |
| c AD = 19,810 m | 42 |
| d AD = 21,030 m | 42 |
| 17 Mass-flow rate through fluidic generator of C1 (as calculated for various assumptions) . . | 44 |
| 18 Mass-flow rate as calculated for flow model 3 as a function of pressure drop across exhaust ports | 46 |
| a AD = 18,290 m | 46 |
| b AD = 19,200 m | 46 |

FIGURES. (Cont'd)

| | <u>Page</u> |
|---|-------------|
| c AD = 19,810 m | 46 |
| d AD = 21,030 m | 46 |
| 19 Comparison of external pressure distribu- tions for C1 and C2; AD = 18,290 m | 49 |
| 20 Internal pressure distribution for C2; AD = 18,290 m | 50 |
| 21 Comparison of mass-flow rates for C1 and C2; $M_{\infty} = 1.13$ | 52 |
| 22 External pressure distribution for C1 at $\alpha = 5^{\circ}$, AD = 19,200 m | 53 |
| 23 Effect of angle of attack on mass-flow rate for C1 | 54 |
| 24 Flow field | 56 |

TABLES

| | |
|--|----|
| 1 Location of the Pressure Taps (Internal and External) | 13 |
|--|----|

1. INTRODUCTION

An experimental program has been conducted to evaluate the performance of the fluidic generator fuze assembly of the Army's Multi-Launch Rocket System (MLRS) in the transonic speed range. The test program, which was conducted in the Aerodynamic Wind Tunnel (4T) at the Arnold Engineering Development Center (AEDC), used full-scale models of the standard nose cone. The test conditions included free-stream Mach numbers from 0.95 to 1.3 over a range of free-stream densities simulating altitudes (AD) from 15,240 m to 21,030 m. Although the primary objective of the test program was to evaluate the flow parameters of the fuze ogive, most of the twelve "different" configurations tested made use of the standard nose cone. The principal variable for six of these configurations was the generator.

However, the primary objective of the present study was to define what parameters affect the flow field (both for the external flow and the internal flow). Since no flow-visualization measurements were made during these tests, the static surface pressures (both for the external surface and the internal surface) are the data of principal interest to this report. The standard nose cone was the most thoroughly instrumented and tested configuration. Therefore, the data analysis and interpretation presented in this report will concentrate on this configuration.

DELIBERATELY BLANK

2. EXPERIMENTAL PROGRAM

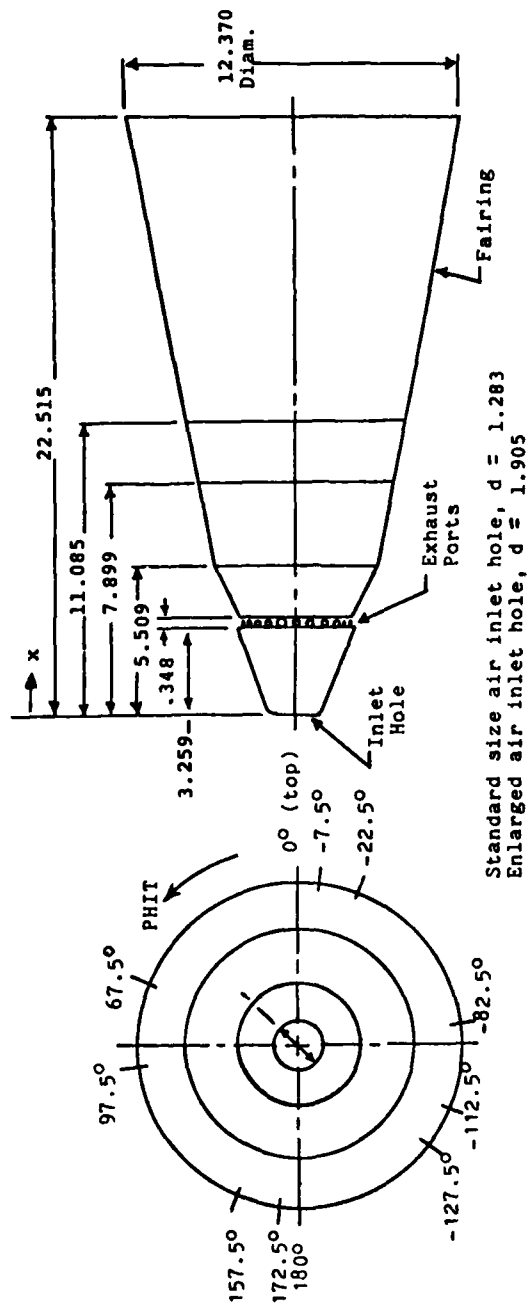
The general features of the standard nose cone are illustrated in the sketches presented in figure 1. The details of the external geometry are presented in figure 1a, with the details of the generator installation in figure 1b. The air that drives the fluidic generator enters the "inlet hole" in the stagnation region of the blunt face and exhausts through a group of 24 ports that are 0.269 cm in diameter. The exhaust ports, which are distributed circumferentially (and equally spaced), are located in a shallow cavity that begins 3.259 cm ($x = 0.423 x_0$) aft of the tip of the fuze. As shown in figure 1, x is the longitudinal position, as measured from the model nose. The reference length, x_0 , was chosen to be 7.696 cm, the coordinate of the most-downstream pressure tap.

The air flow which enters the inlet hole in the stagnation region of the flat face (fig. 1a) passes through the generator assembly and into the (internal) chamber (fig. 1b). It then flows through the exhaust ports (fig. 1a) into the (external) cavity (fig. 1b). This use of the words "chamber" for the internal region and "cavity" for the external will be retained throughout this report.

Static-pressure measurements and Pitot-pressure measurements will be presented for four configurations. The geometry for all four configurations is essentially that for the standard nose cone, as presented in figure 1. Data are presented for the following configurations:

- Configuration 1 (C1): the standard nose cone,
- Configuration 2 (C2): the standard nose cone with an ogive angle adapter installed (as shown in fig. 1c),
- Configuration 4 (C4): the standard nose cone with the inlet plugged, and
- Configuration 9 (C9): the standard nose cone with a total-head pressure probe in the inlet hole.

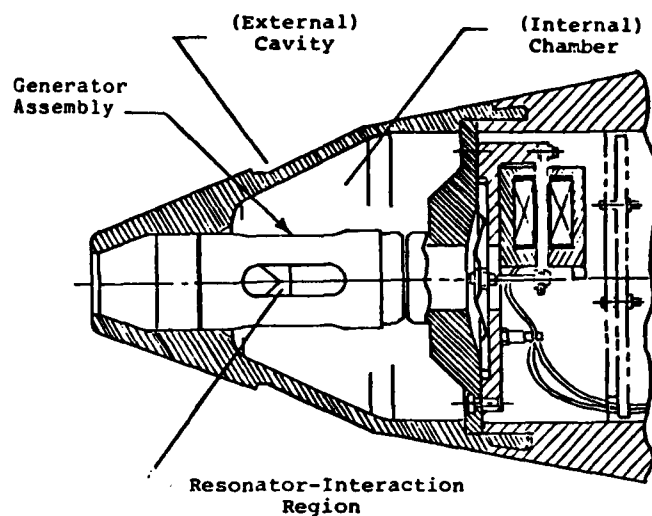
The standard nose cone used in the initial phase of the test program was instrumented with 29 surface pressure taps (or orifices), of which 21 were on the external surface and 8 were on the internal surface. The locations of these ori-



Dimensions in cm

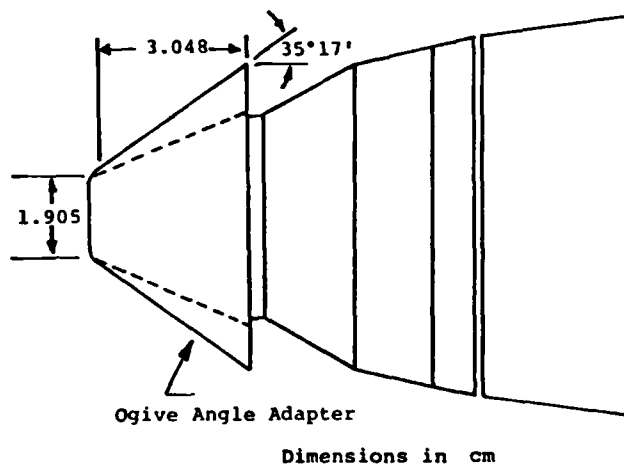
(a) External geometry

Figure 1. Sketch of the Army/MLRS Fluidic-Generator Fuze-Assembly.



(b) Details of Generator Installation

Figure 1. Continued.



(c) Details and Installation of Fuze Ogive Adapter (Configuration 2)

Figure 1. Concluded.

fices are presented in table 1. Fine¹ compared the pressure readings at a particular location at the same flow condition as measured during different runs (both with the same generator and with different generators). Fine, citing pressure variations at a given orifice location of +1.5 percent, or less, noted that "the measurements were consistent and repeatable at the same tunnel conditions." Furthermore, the "repeatability also indicates that the differences in the nozzle configurations in the three generators did not affect the pressures that were measured."

For additional information about the wind tunnel, the model, the data reduction techniques, or other details about the test program, the reader is referred to the test report of Hodges.²

¹J. E. Fine, *Preliminary Analysis of Pressure Measurements in MLRS Nov. 80 Wind Tunnel Test, DELHD-DE-OP, Jan 1981, HDL Office Memo.*

²D. A. Hodges, *Performance Evaluation of the XM-445 Fluidic Generator Fuze Assembly at Mach Numbers from 0.95 to 1.3, AEDC-TSR-80-P81, Dec. 1980, AEDC.*

TABLE I. LOCATION OF THE PRESSURE TAPS (INTERNAL AND EXTERNAL)

| Tap | Surface location | PHIT† | x (cm) | x (in) | x/x ₀ |
|------|------------------|------------|--------|--------|------------------|
| 11 | External ↓ | 0. | 0.229 | 0.090 | 0.030 |
| 12 | | ↓ | 1.638 | 0.645 | 0.213 |
| 13 | | ↓ | 2.344 | 0.923 | 0.305 |
| 14 | | ↓ | 3.048 | 1.200 | 0.396 |
| 15 | | -7.5 | 3.259 | 1.283 | 0.423 |
| 16 | | ↓ | 3.409 | 1.342 | 0.443 |
| 17 | | 0. | 3.708 | 1.460 | 0.482 |
| 18 | | ↓ | 4.242 | 1.670 | 0.551 |
| 19 | | ↓ | 4.775 | 1.880 | 0.620 |
| 20 | | ↓ | 5.306 | 2.089 | 0.689 |
| 21 | | ↓ | 5.712 | 2.249 | 0.742 |
| 22 | | ↓ | 7.696 | 3.030 | 1.000 |
| 23 | Internal ↓ | 67.5 | 3.048 | 1.200 | 0.396 |
| 24 | | ↓ | 3.708 | 1.460 | 0.482 |
| 25 | | -22.5 | 0.203 | 0.080 | 0.026 |
| 26 | | ↓ | 1.016 | 0.400 | 0.132 |
| 27 | | ↓ | 3.124 | 1.230 | 0.406 |
| 28 | | -7.5 | 4.445 | 1.750 | 0.576 |
| 29 | | ↓ | 5.969 | 2.350 | 0.775 |
| 30 | | ↓ | 7.163 | 2.820 | 0.931 |
| 31 | | -82.5 | 0.000 | 0.000 | 0.000 |
| 113 | | 180. | 2.344 | 0.923 | 0.305 |
| 115 | External ↓ | 172.5 | 3.259 | 1.283 | 0.423 |
| 116 | | ↓ | 3.409 | 1.342 | 0.443 |
| 117 | | 180. | 3.708 | 1.460 | 0.482 |
| 120 | | ↓ | 5.306 | 2.089 | 0.689 |
| 125 | | 157.5 | 0.203 | 0.080 | 0.026 |
| 128 | | ↓ | 4.445 | 1.750 | 0.577 |
| 131 | | 97.5 | 0.000 | 0.000 | 0.000 |
| 32* | | Total Head | -112.5 | 0.080 | 0.026 |
| 132* | | 67.5 | ↓ | ↓ | ↓ |

† See figure 1a.

* Pitot - Probe for C9.

DELIBERATELY BLANK

3. RESULTS

Static pressures and Pitot pressures were measured both on the external surface and on the internal surface of a full-scale fluidic generator/fuze assembly of the MLRS in the Aerodynamic Wind Tunnel (4T) at AEDC. The pressure data from these tests are discussed in this section.

3.1 External Pressures for 0° Angle of Attack

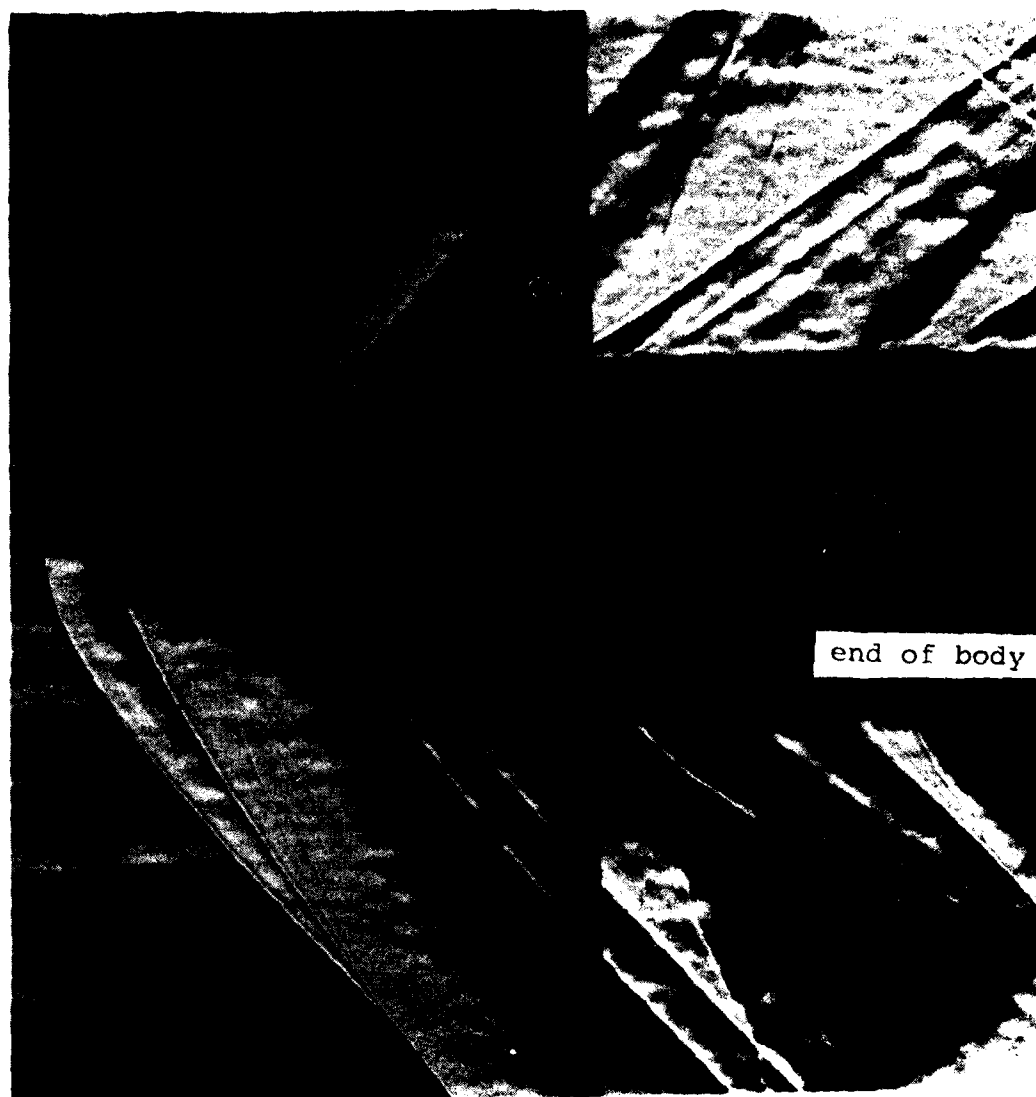
3.1.1 Pressures on Flat Face ($x = 0.0$)

A strong, detached shock wave forms in front of a blunt body when it is placed in a supersonic stream. The shape of the bow shock wave for supersonic flow past a nose-cone configuration like that of C1 is shown in the Schlieren photographs from a previous test program³ that are presented in figure 2. Since the Mach numbers of the flows represented by the Schlieren photographs are greater than those of the present program, the stand-off distance of the bow shock wave is much less than would be the case for the present flows. This is to be expected. Nevertheless, the photographs provide valuable insights into the flow. Because the bow shock wave is curved, the static pressure on the surface should decrease from a value of the stagnation pressure downstream of a normal shock wave, p_{t2} , at the axis of symmetry to the sonic value at the corner. This pressure variation is illustrated by the pressure distribution that was presented elsewhere⁴ for a free-stream Mach number, M_∞ , of 2.01 (see fig. 3). The pressure distributions for the present tests will be similar to that of figure 3 despite the difference in Mach number.

Included with the pressure distributions in figure 3 are the pressure-instrumentation locations for these models. As can be seen from figures 1 and 3 and table 1, two static-

³R. L. Goodyear and H. Lee, *Performance of the Fluidic Power Supply for the XM-445 Fuze in Supersonic Wind Tunnels*, HDL-TM-81-4, Feb. 1981, Harry Diamond Laboratories.

⁴J. C. Boison and H. A. Curtiss, *An Experimental Investigation of Blunt Body Stagnation Point Velocity Gradient*, ARS Journal, Feb. 1959, Vol. 29, No. 2, pp. 130-135.



(a) $M_{\infty} = 1.5$

Figure 2. Schlieren photographs from the tests of ref. 3.



(b) $M_{\infty} = 5$

Figure 2. Concluded.

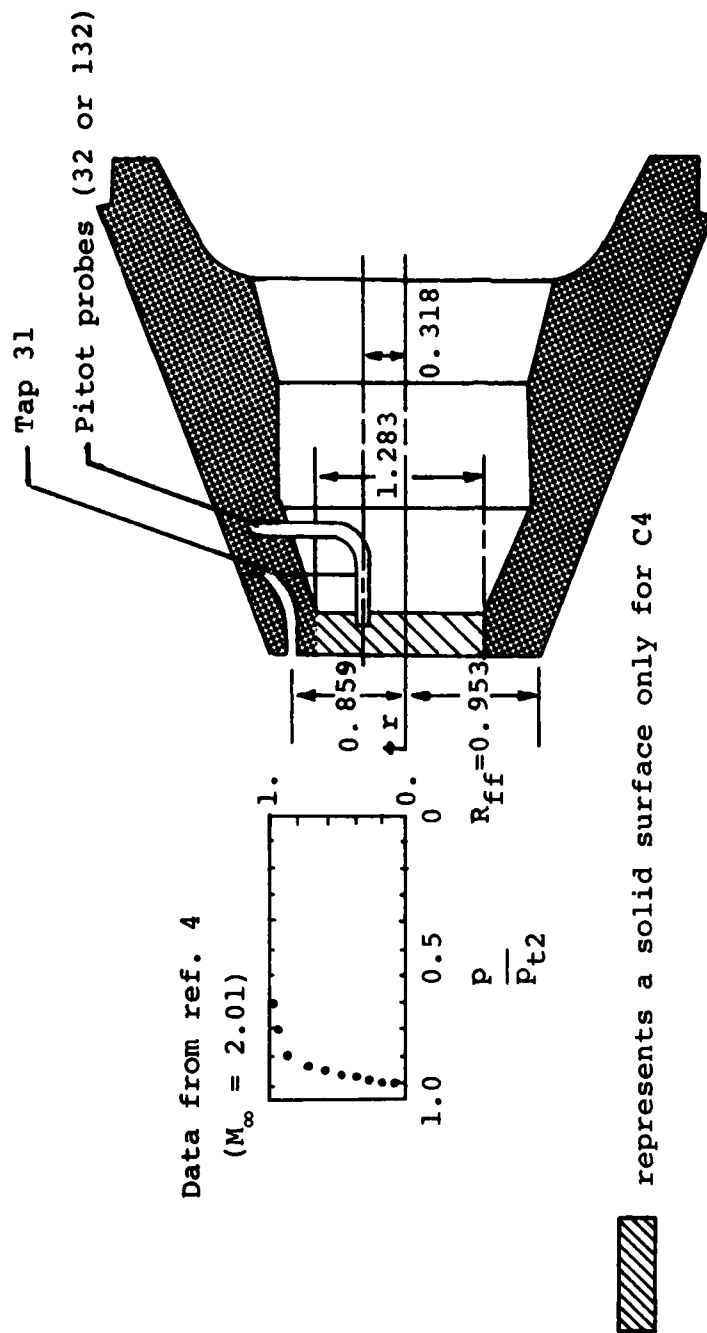


Figure 3. Location of pressure sensors for C1, C4, and C9 and sketch of pressure distribution for a flat-faced cylinder (ref. 4).

pressure orifices were on the flat face of the nose cone, between the inlet hole and the corner radius. One of these, tap 31, was approximately 0.859 cm from the axis of symmetry, i.e., $r = 0.90 R_{ff}$. The experimentally determined pressure coefficients, C_p , for this orifice are presented in figure 4 for C1 at density altitudes of 18,290 m and 21,030 m and for C4 at a density altitude of 18,290 m. Included are the experimental C_p for the two total-pressure probes that were 0.318 cm from the axis, in the inlet hole of C9. These experimentally determined C_p are compared with theoretical C_p , as calculated for the flow downstream of a normal shock wave, using the relation

$$C_{p,t2} = \left[\frac{p_{t2}}{p_{\infty}} - 1 \right] \frac{2}{\gamma M_{\infty}^2}, \quad (1)$$

where $C_{p,t2}$ is the stagnation pressure coefficient, p_{∞} is free-stream static pressure, and γ is the ratio of specific heats. The ratio p_{t2}/p_{∞} was determined as a function of M_{∞} using normal shock wave tables.⁵

The experimental C_p determined using the Pitot probes in the inlet hole (C9) are in very good agreement with the theoretical values. This is to be expected, since the probes are near the axis of symmetry (where the bow shock wave is most nearly normal) and, being Pitot probes, they provide a measure of the stagnation pressure. The surface static pressures at tap 31 are below the theoretical predictions. This is also to be expected. When a flat-faced cylinder with a "slender" conical afterbody is exposed to a supersonic stream, the bow shock wave is curved and the sonic "line" is fixed at the corner of the flat-faced portion of the nose cone. As a result, the static pressure decreases with r over the flat face from the "stagnation pressure" at the axis of symmetry to the sonic value at the corner. Using the data presented in figure 3 (which are for $M_{\infty} = 2.01$), one would expect the local static pressure at $r = 0.90 R_{ff}$ to be approximately 0.9 p_{t2} . As a result, the C_p for this orifice would be approximately 1.22 when $M_{\infty} = 1.3$. This value is in reasonable agreement with the data of figure 4, considering the difference in the free-stream Mach numbers. It is interest-

⁵ Ames Research Staff, *Equations, Tables, and Charts for Compressible Flow*, Report 1135, 1953, National Advisory Committee for Aeronautics (NACA).

- Tap 31, Configuration 1, AD = 18,290 m.
- △ Tap 31, Configuration 1, AD = 21,030 m.
- Tap 31, Configuration 4, AD = 18,290 m.
- Tap 32, Configuration 9, AD = 18,290 m.
- ⊙ Tap 132, Configuration 9, AD = 18,290 m.

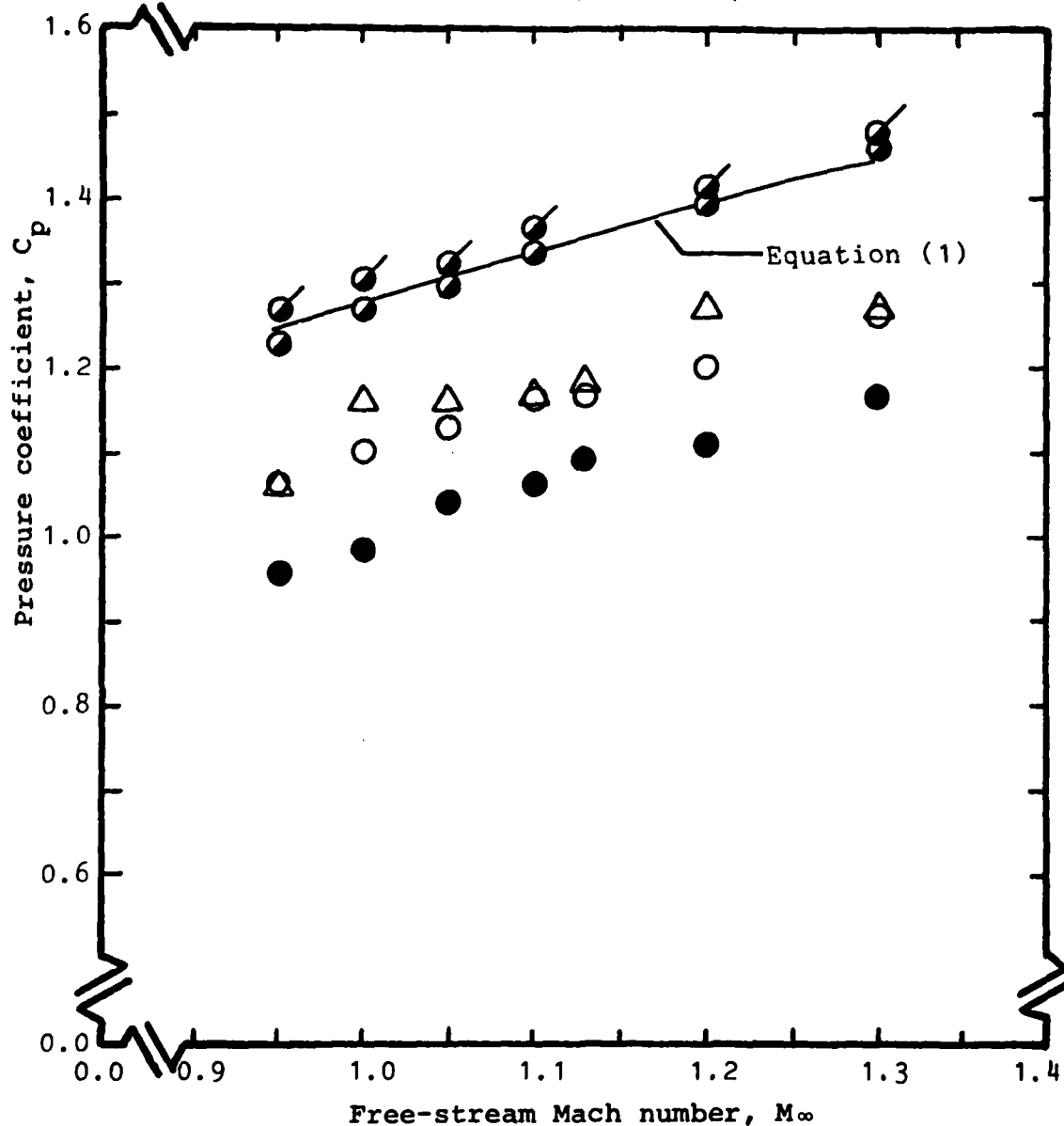


Figure 4. Pressure coefficients for flat face as a function of free-stream Mach number.

ing to note that the pressures are higher for C1 (with an inlet hole) than for C4 (the plugged configuration). Apparently, because some of the air passes through the vent hole, the stand-off distance for the bow shock wave is less for C1; therefore, the shock is more nearly normal (stronger) over a greater radial distance. This is illustrated by the proposed flow models presented in figure 5.

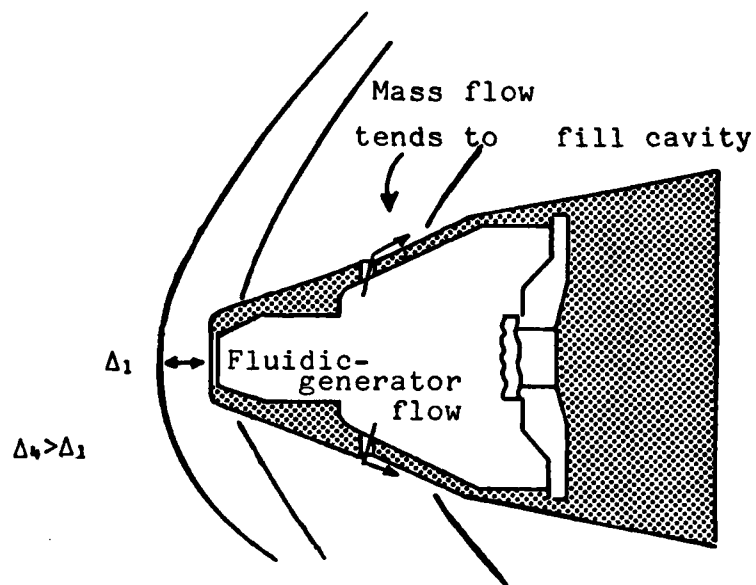
3.1.2 Pressures on Conical Surface of Ogive

Additional information about the flow field can be determined from the Schlieren photographs in figure 2. Of interest is the flow over the first (forward) conical segment at a free-stream Mach number, M_∞ , of 1.50. A rapid expansion of the flow just past the corner is terminated by a shock wave at $x = 0.1 x_0$. It is assumed that the shock wave results when the flow external to a separation bubble (which exists at the corner) turns when it reattaches to the surface. Furthermore, although the cavity (containing the exhaust ports) is relatively long, the flow appears to "jump over" the cavity; i.e., the cavity is open. This conclusion is based both on what appears in the photograph for the cavity-region flow and what does not appear: there is no recompression shock wave near the end of the cavity. For the Mach 5 flow, a recompression shock wave near the midpoint of the cavity indicates that the cavity is closed. As will be discussed, the pressure data from the present tests indicate that the flow does not "jump over" the cavity since there is a (weak) recompression of the flow near the midpoint of the cavity.

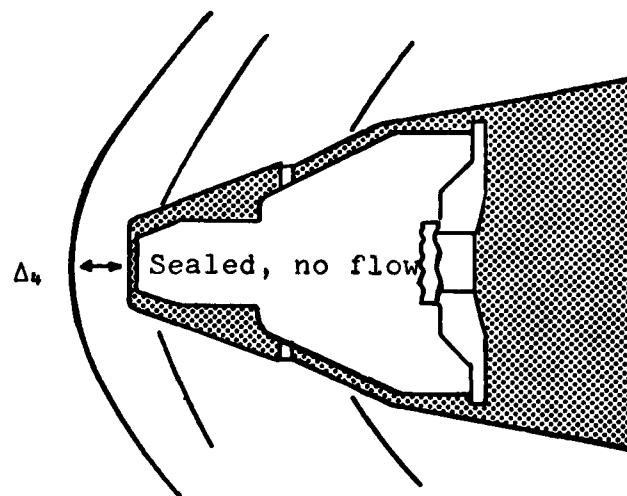
The detailed sketch of the external geometry of the nose cone, presented in figure 6, illustrates the locations of the pressure taps and some features of a proposed model for the external flow. Although the flow expands (accelerates) rapidly around the corner, it cannot accelerate fast enough to remain attached to the surface, and a separation bubble forms at the corner. This assumption is supported by the pressures at the orifice in the "separated region" (at $x = 0.030 x_0$) which are relatively low (see fig. 7).

Downstream of the separation bubble, the flow over the external surface of the nose cone was calculated using two different approaches. Theoretical C_p were calculated using standard normal shock-wave tables and graphs for sharp cones. Values are presented

- (1) for the stagnation point ($C_p = 1.45$),
- (2) for the forward conical segment ($C_p = 0.48$, the



(a) Configuration 1



(b) Configuration 4

Figure 5. Flow models for (low) supersonic flow over standard nose cone.

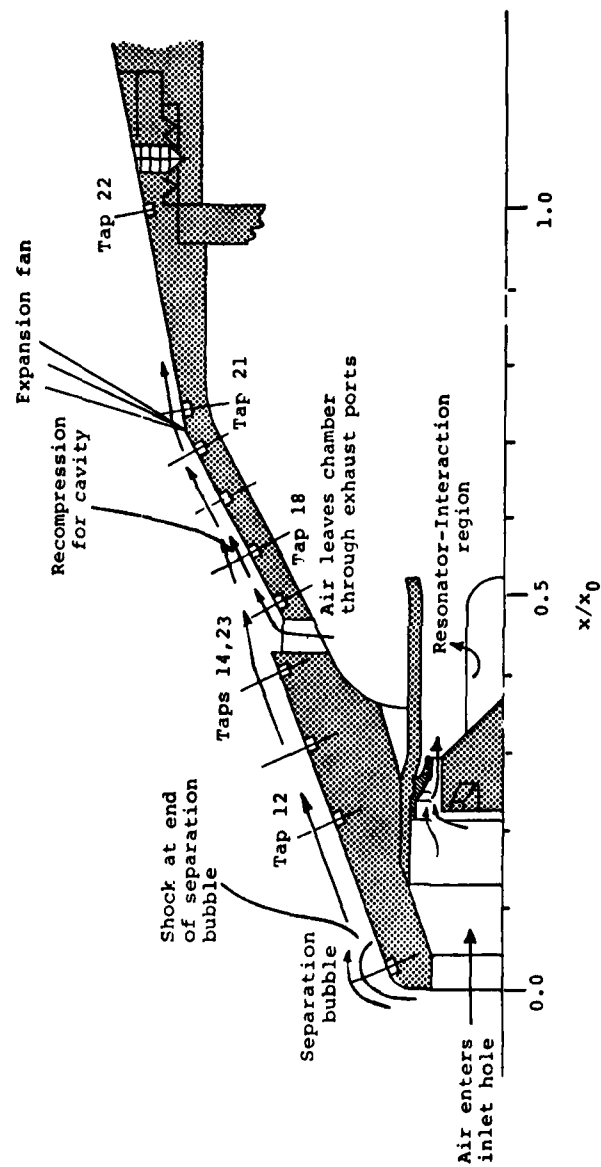


Figure 6. Proposed flow model and relation between flow phenomena and instrumentation.

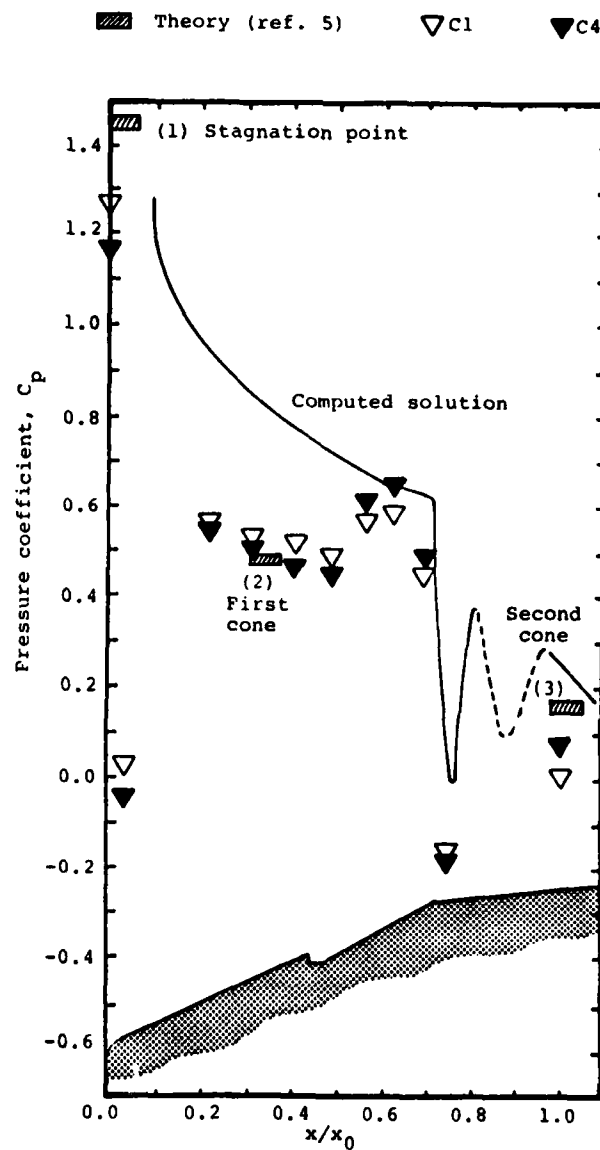


Figure 7. Comparison between theoretical and experimental pressure distributions, $M_\infty = 1.3$, $AD = 18,290$ m, $\alpha = 0^\circ$.

- value for a sharp cone whose half-angle is 20.5°),
and
(3) for the second conical segment ($C_p = 0.16$, the value
for a sharp cone whose half-angle is 10.75°).

Also included is the theoretical distribution computed using the University of Texas' Missile Aerodynamics Code, which is similar to that described by Moore and Swanson⁶. In preparing the geometric input for the computer solution, the presence of the cavity in the external contour was omitted; the nose cone was represented by two conical frustums. Because of the extreme bluntness of the nose cone, the computed solution should also be considered approximate.

Included for comparison with the theoretical pressures in figure 7 are the experimentally determined C_p distributions for $M = 1.3$ at a density altitude of 18,290 m, with an angle of attack of 0° for C1 and C4. All the pressure measurements are for orifices (pressure taps) in the $PHIT = 0^\circ$ plane, except for the tap at $x = 0.396 x_0$ (tap 23). The data for tap 23 ($PHIT = 67.5^\circ$) were used at this location, since a leak was observed for tap 14, the 0° gage, in a post-test investigation.

The comparison between the experimental and the theoretical C_p on the flat face has already been discussed (see fig. 4). Both the computed solution and the "sharp-cone" approximations⁵ provide a reasonable estimate of the pressures on the downstream (second) conical segment, i.e., for $x \geq 0.716 x_0$. The computer solution even predicts the rapid "overexpansion" that takes place downstream of the intersection of the two conical segments.

An oscillatory character which appeared in the computed solution for the pressure distribution for the second conical segment is represented in figure 7 by a broken line. The broken-line representation was used since the variation may be a computational peculiarity and not a flow phenomenon.

⁶F. G. Moore and R. C. Swanson, Jr., *Aerodynamics of Tactical Weapons to Mach Number 3 and Angle of Attack 15°* , Part I--Theory and Application, NSWC/DL TR-3584, Feb. 1977, Naval Surface Weapons Center.

⁵Ames Research Staff, *Equations, Tables, and Charts for Compressible Flow*, Report 1135, 1953, National Advisory Committee for Aeronautics (NACA).

The most significant differences between the theoretical values and the experimental values occur on the forward conical surface and in the cavity in this region. Note that the upstream edge of the cavity is at $x = 0.423 x_0$. The experimental pressures at the first tap of the cavity (tap 17 at $x = 0.482 x_0$) are essentially equal to those upstream of the cavity. The fact that the pressure did not decrease when the flow separated at the cavity is attributed to the relatively shallow depth of the cavity. The pressure increase at the three pressure taps in the downstream region of the cavity ($0.551 x_0 \leq x \leq 0.689 x_0$) reflects the recompression of the flow as it reattaches to the surface. Thus, if one assumes that a tangent-cone approximation is valid for the forward conical surface and that a recompression pressure rise occurs at the downstream end of the cavity, one can explain the fact that the pressures measured at the taps between $0.551 x_0$ and $0.689 x_0$ are above the Ames theoretical estimates⁵. Since both theoretical models are approximate, close correlation with the data should not be expected. Each assumed model probably contains elements of the actual flow field.

In this test program, the tunnel was operated in two different modes: Mach number sweeps and density altitude sweeps. The density altitude sweeps were made from 15,240 m to 21,030 m at a Mach number of 1.13. To decide whether there is an effect from varying the density altitude, consider the data presented in figures 8 through 10. Pressure ratios p/p_{t2} (where p is static pressure and p_{t2} is stagnation pressure) are presented over the test range of density altitudes for each of the three Mach numbers (covering the complete test range) at three orifice locations:

- (a) $x = 0.213 x_0$, near the midpoint of the forward cone (tap 12 of fig. 6),
- (b) $x = 0.396 x_0$, the last orifice upstream of the cavity (tap 23 of fig. 6), and
- (c) $x = 0.551 x_0$, near the midpoint of the cavity (tap 18 of fig. 6).

Figure 6 shows the location of these taps in relation to the physical features of the external surface and the flow field. For $x = 0.396 x_0$, pressure measurements are presented for the orifice in the $\text{PHIT} = 67.5^\circ$ plane.

⁵ Ames Research Staff, *Equations, Tables, and Charts for Compressible Flow*, Report 1135, 1953, National Advisory Committee for Aeronautics (NACA).

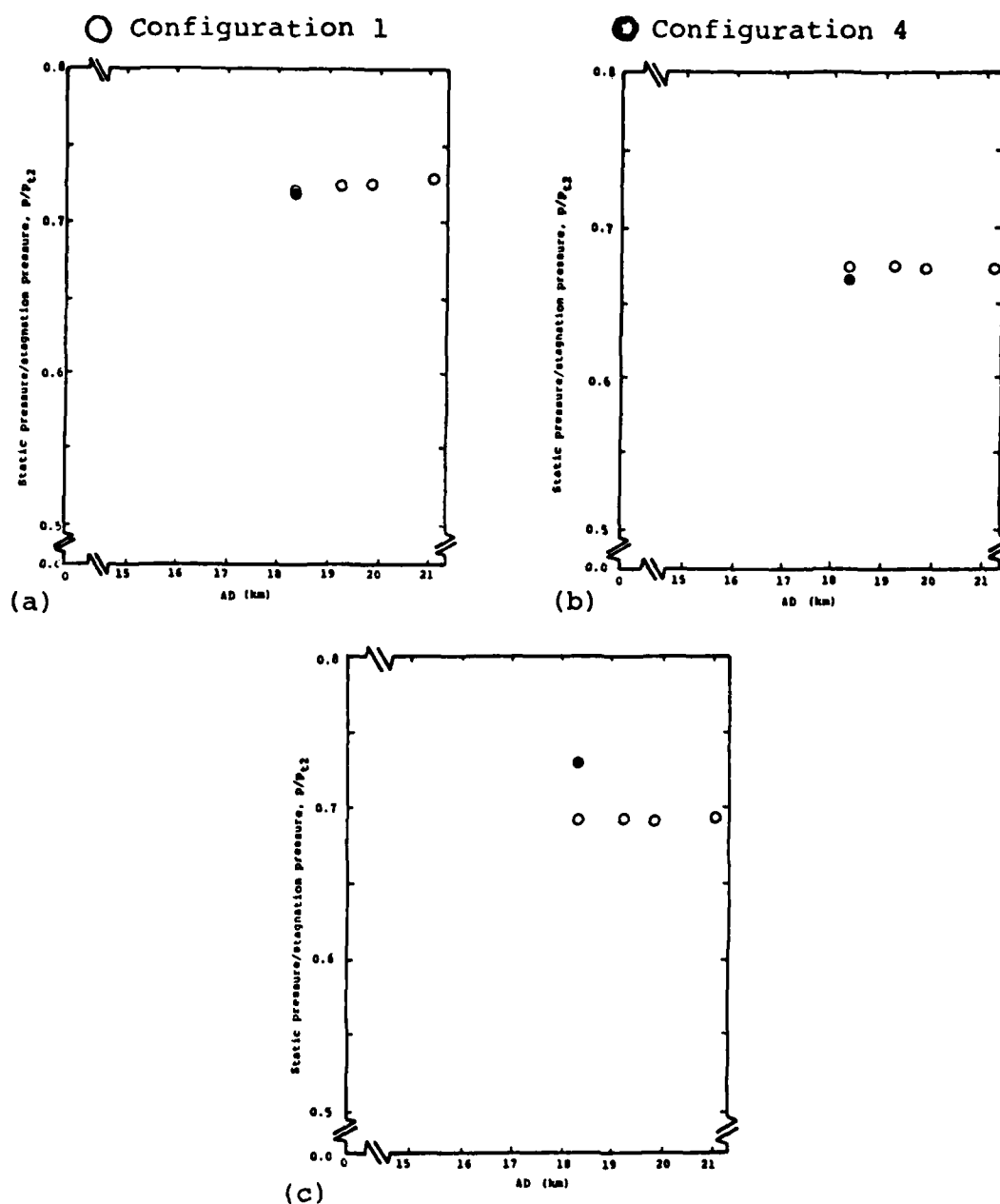


Figure 8. Effect of density altitude (AD) on local static pressure for $M_{\infty} = 0.95$:
 (a) $x = 0.213 x_0$ (tap 12), (b) $x = 0.396 x_0$ (tap 23), and (c) $x = 0.551 x_0$ (tap 18).

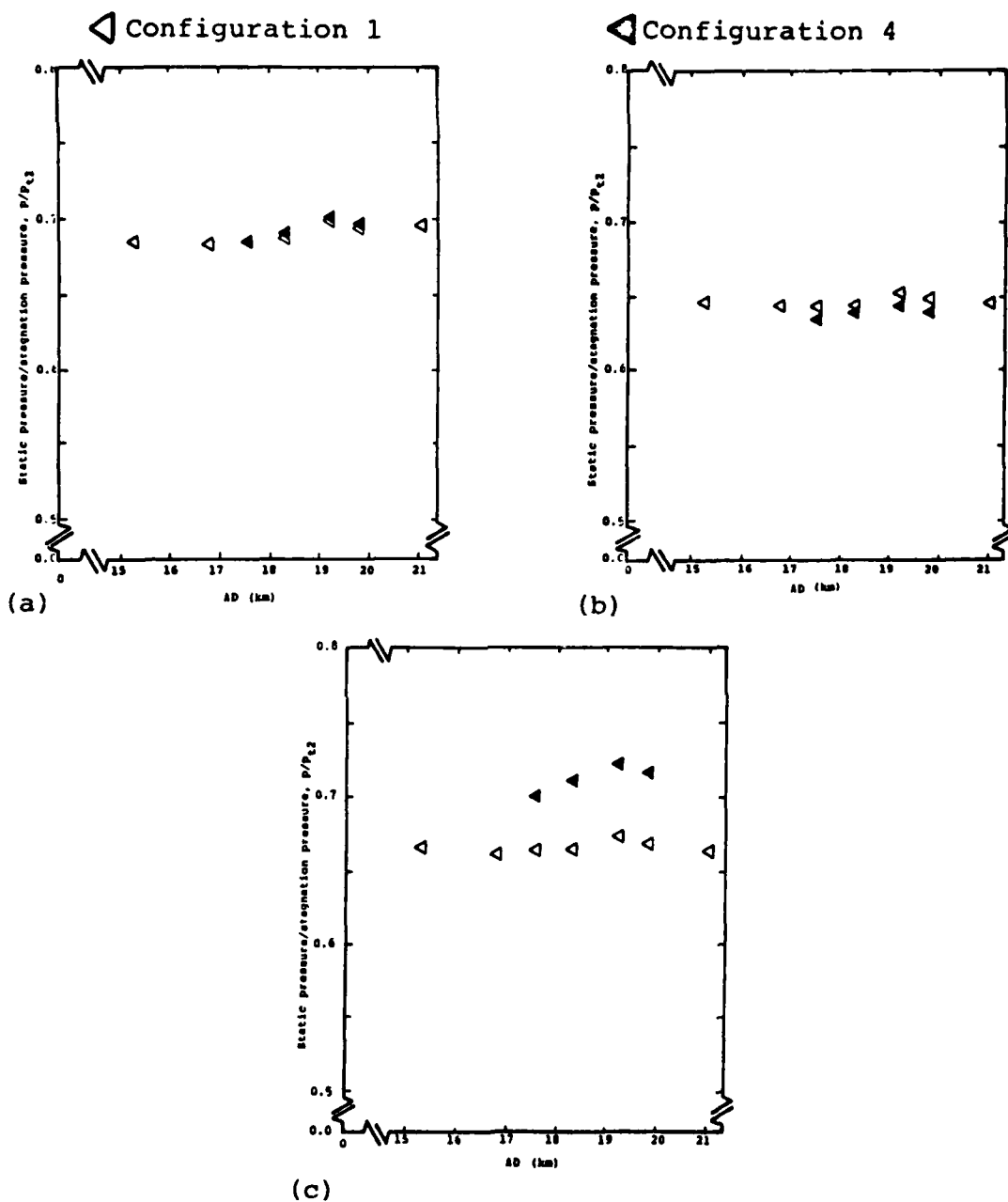


Figure 9. Effect of density altitude (AD) on local static pressure for $M_\infty = 1.13$:
 (a) $x = 0.213 x_0$ (tap 12), (b) $x = 0.396 x_0$ (tap 23), and (c) $x = 0.551 x_0$ (tap 18).

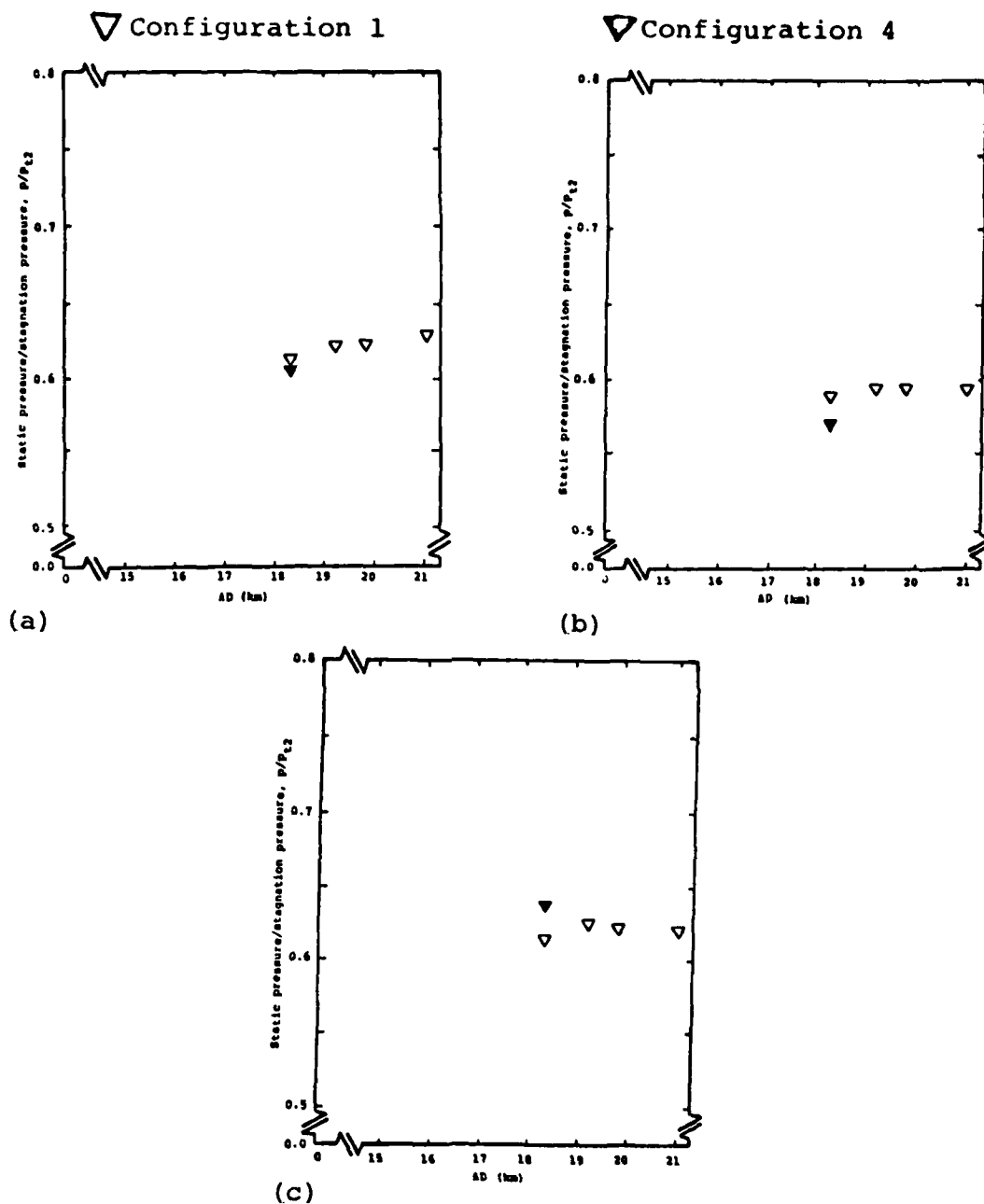


Figure 10. Effect of density altitude (AD) on local static pressure for $M_{\infty} = 1.3$.
 (a) $x = 0.213 x_0$ (tap 12), (b) $x = 0.396 x_0$ (tap 23), and (c) $x = 0.551 x_0$ (tap 18).

Since the trends exhibited by the data appear to be the same for all three Mach numbers, the discussion of the data is the same for each figure. Referring to figure 7, the pressures measured at the orifice at $x = 0.551 x_0$ are significantly higher than those measured at the previous orifice (tap 17 at $x = 0.482 x_0$, which is also in the cavity). Because the cavity is relatively long, this "sudden" pressure rise is attributed to a recompression (however mild) due to the reattachment of the free-shear layer. Since the pressure rise depends on the character of the free-shear layer, the data from this orifice should be most sensitive to the density altitude or, equivalently, the Reynolds number. Nevertheless, no effect of density altitude (and, therefore, of the Reynolds number) is evident in the data. It is interesting to note, however, that the pressures measured at this orifice for C4, for which the inlet hole is sealed, are consistently greater than those for C1. This is true for the other two orifices in the "recompression" region (see fig. 7). Thus, the air which enters the inlet hole and exhausts through the vent ports tends to fill the cavity and to further diminish the strength of the recompression associated with the reattaching shear layer. This feature of the flow is included in the flow model illustrated in figures 5 and 6.

Distributions of the static pressures measured on the external surface (divided by p_{t2}) are presented in figure 11 for a density altitude of 18,290 m. In each part of the figure, data are presented for C1 and C4 at a particular Mach number, covering the complete Mach-number range of the test program. Note that, although different dimensionless pressure parameters are used, the data presented in figure 11d are the same as those presented in figure 7. For all orifices upstream of $x = 0.49 x_0$, the pressures of C1 are greater than those of C4. Based on the assumed flow model, these pressures apparently reflect the effect of the inlet hole on the shape of the bow shock wave. However, for the orifices in the aft region of the cavity (those for x from $0.551 x_0$ to $0.689 x_0$), the pressures for C4 are greater. The differences between the pressures in this region for the two configurations are attributed to the air flow that activates the fluidic generator. The data indicate that the air flow for C1 enters the external cavity through the exhaust ports and "fills" the cavity. Thus, the flow turns through a smaller angle during the reattachment of the shear layer, causing a smaller pressure rise. These comments are valid over the entire range of Mach numbers for the present tests. No singularities are evident with changes in the x -coordinate for any of the Mach numbers of figure 11, which cover the entire range of the test program.

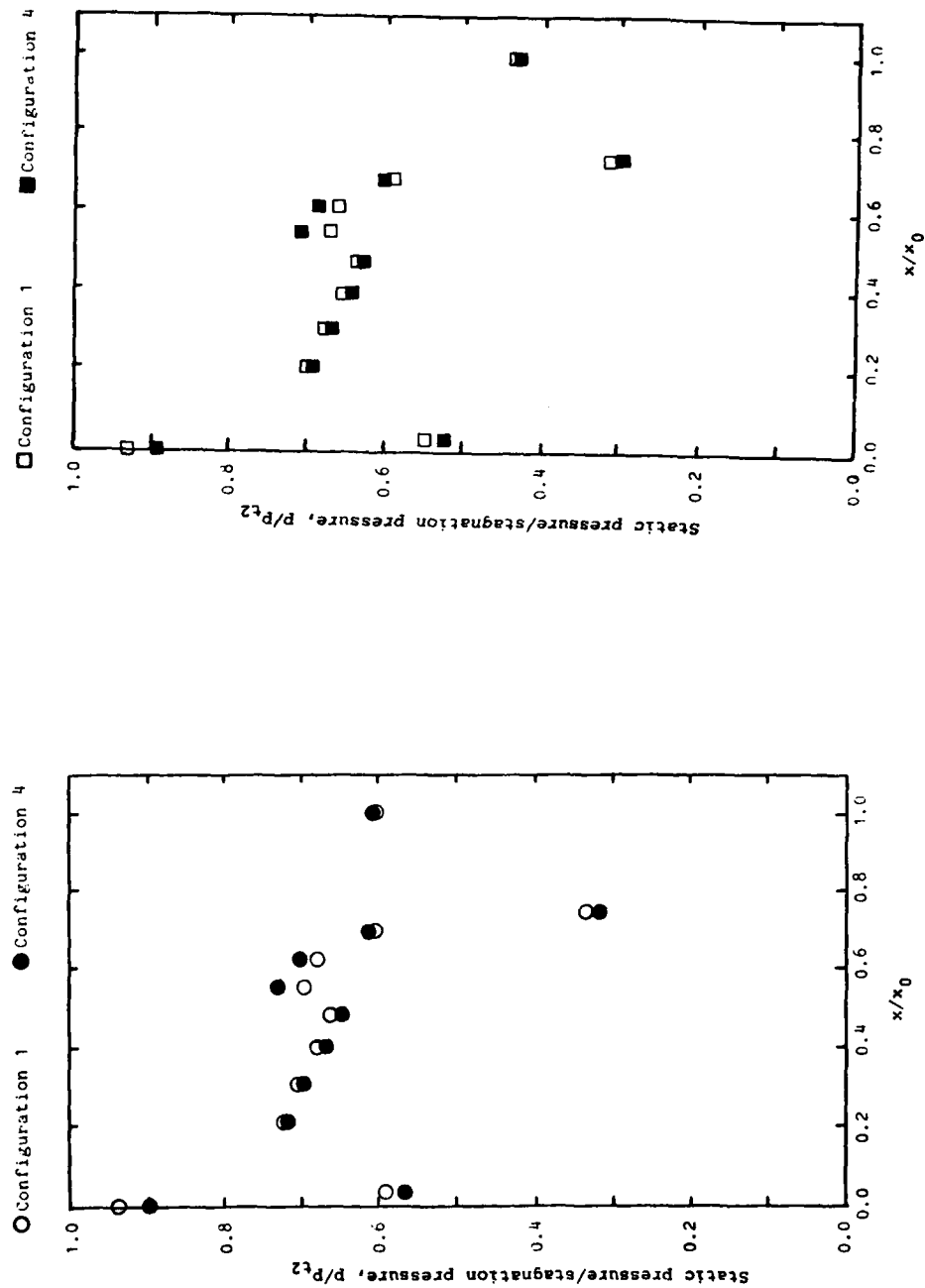


Figure 11. Effect of inlet on pressure distributions for $AD = 18,290$ m:
 (a) $M_\infty = 0.95$, and (b) $M_\infty = 1.1$.

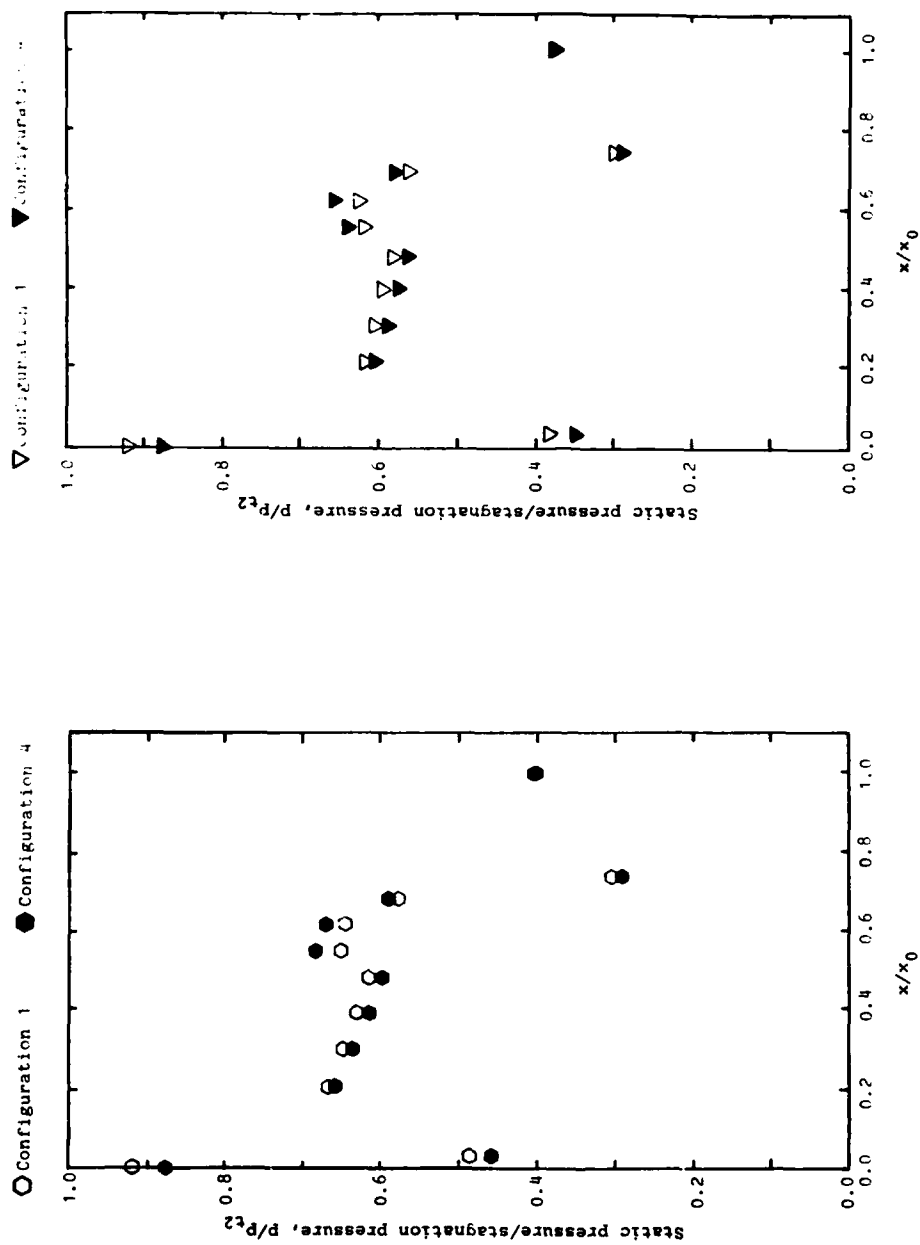


Figure 11. Concluded: (c) $M_\infty = 1.2$, and (d) $M_\infty = 1.3$.

The effect of M_∞ on the pressure distribution is illustrated by the data presented in figures 12 and 13. The pressure distributions for a density altitude of 18,290 m are presented in figure 12, and for 21,030 m in figure 13. There is a consistent trend with Mach number at all the orifices from $x = 0.030 x_0$ to $x = 1.000 x_0$. That is, the ratio p/p_{t2} at a particular orifice decreases as the Mach number increases. The variation is greatest at the two extreme orifices. The Mach-number dependent variation at $x = 0.030 x_0$ indicates a change in the characteristics of the separation bubble for these transonic flows. Furthermore, the pressure ratio varies by almost a factor of two at the last orifice. However, the experimental values of p/p_{t2} at this orifice vary relatively little for $1.1 \leq M_\infty \leq 1.3$. Thus, the spread in the data for the three lowest Mach numbers suggests that a significant change occurs in the downstream region of the flow field for these transonic flows.

The pressure ratio p/p_{t2} for four orifice locations is presented as a function of the free-stream Mach number in figure 14. The first two locations, $x = 0.213 x_0$ and $x = 0.396 x_0$, are on the first conical segment whereas the third orifice, at $x = 0.551 x_0$, is in the downstream portion of the cavity. Despite differences in the local flow fields for these three locations, the pressure ratio (at a given location) decreases as the Mach number increases and is independent of the density altitude. The Mach-number dependence is similar for all three locations.

To establish if this Mach-number dependence has an analytical basis, let us examine the C_p as given by the small deflection approximation for supersonic flow,

$$C_p = \left(\frac{p}{p_\infty} - 1 \right) \frac{2}{\gamma M_\infty^2} = \frac{C_1}{\sqrt{M_\infty^2 - 1}}, \quad (2)$$

where C_1 is a constant (which is dependent on M_∞ and the local flow direction). The equation can be rearranged to yield

$$\frac{p}{p_\infty} = \frac{\gamma C_1 M_\infty^2}{2\sqrt{M_\infty^2 - 1}} + 1. \quad (3)$$

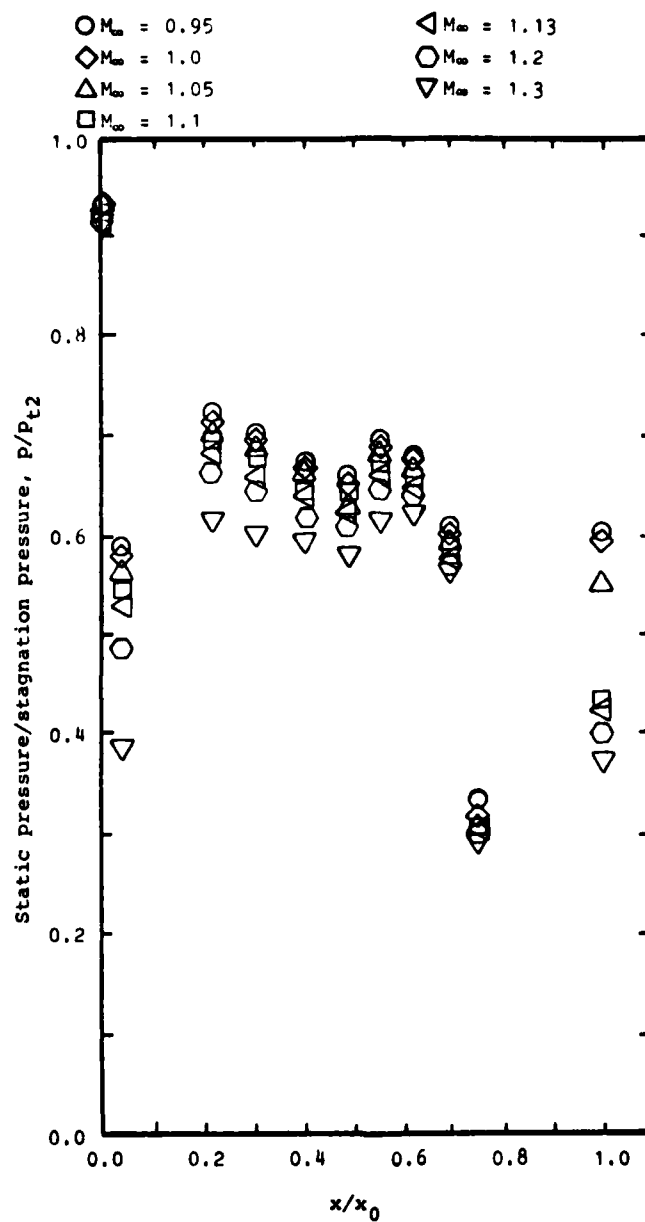


Figure 12. Effect of Mach number on pressure distributions for AD = 18,290 m.

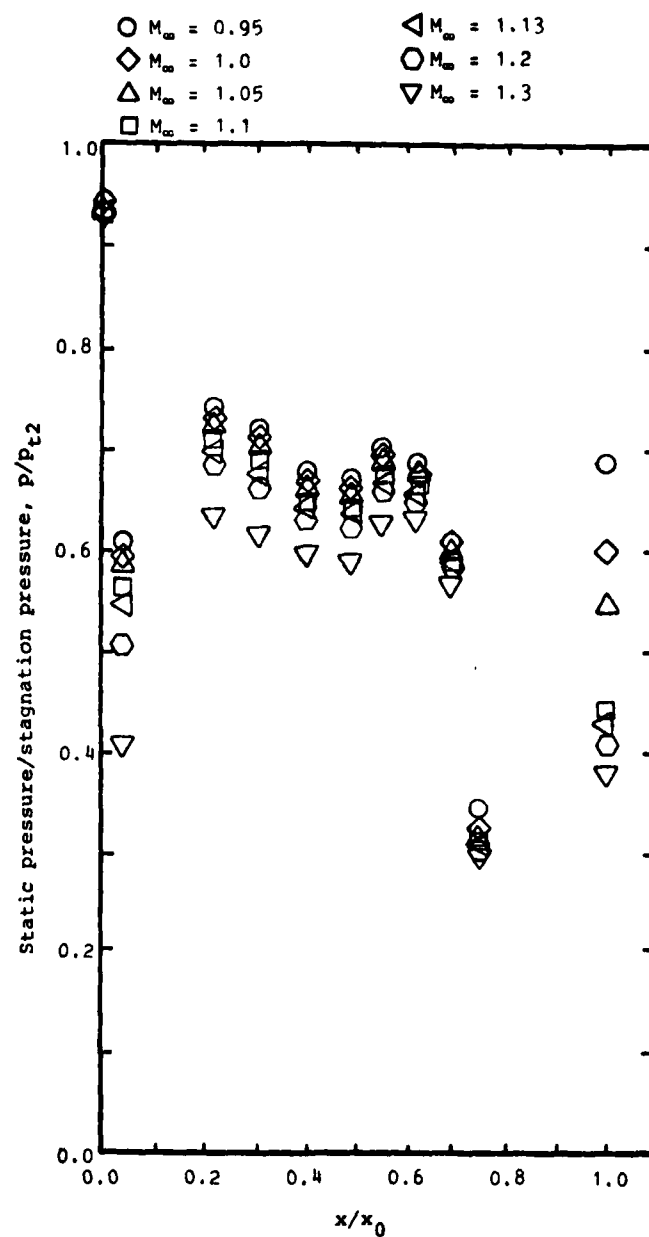


Figure 13. Effect of Mach number on pressure distributions for AD = 21,030 m.

AD: ○ 18,290 m; ◇ 19,200 m; □ 19,810 m; △ 21,030 m.
 Open symbols: C1; Filled symbols: C4.

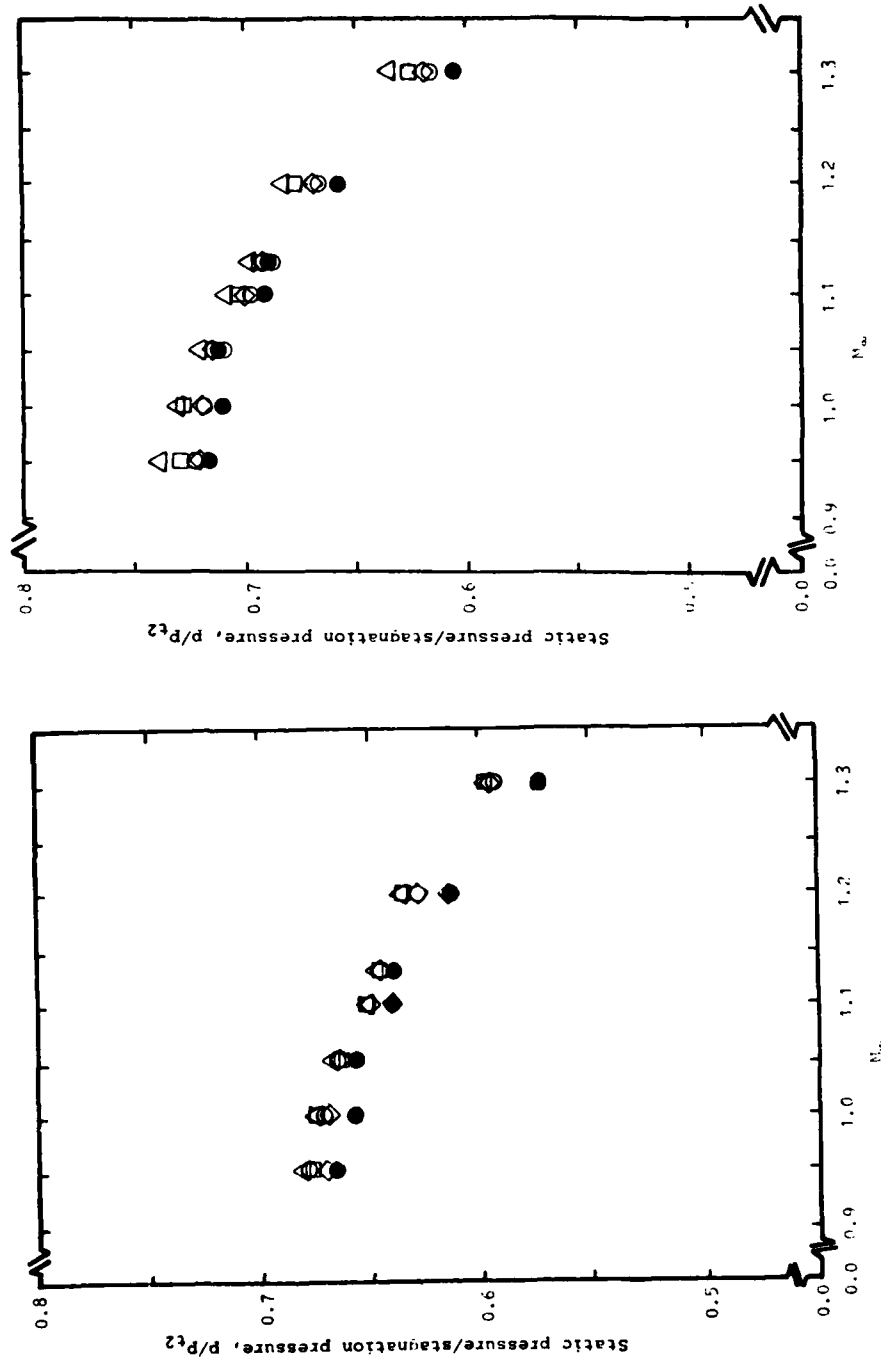


Figure 14. Effect of Mach number on local pressures: (a) $x = 0.213 x_0$ (tap 12), and (b) $x = 0.396 x_0$ (tap 23).

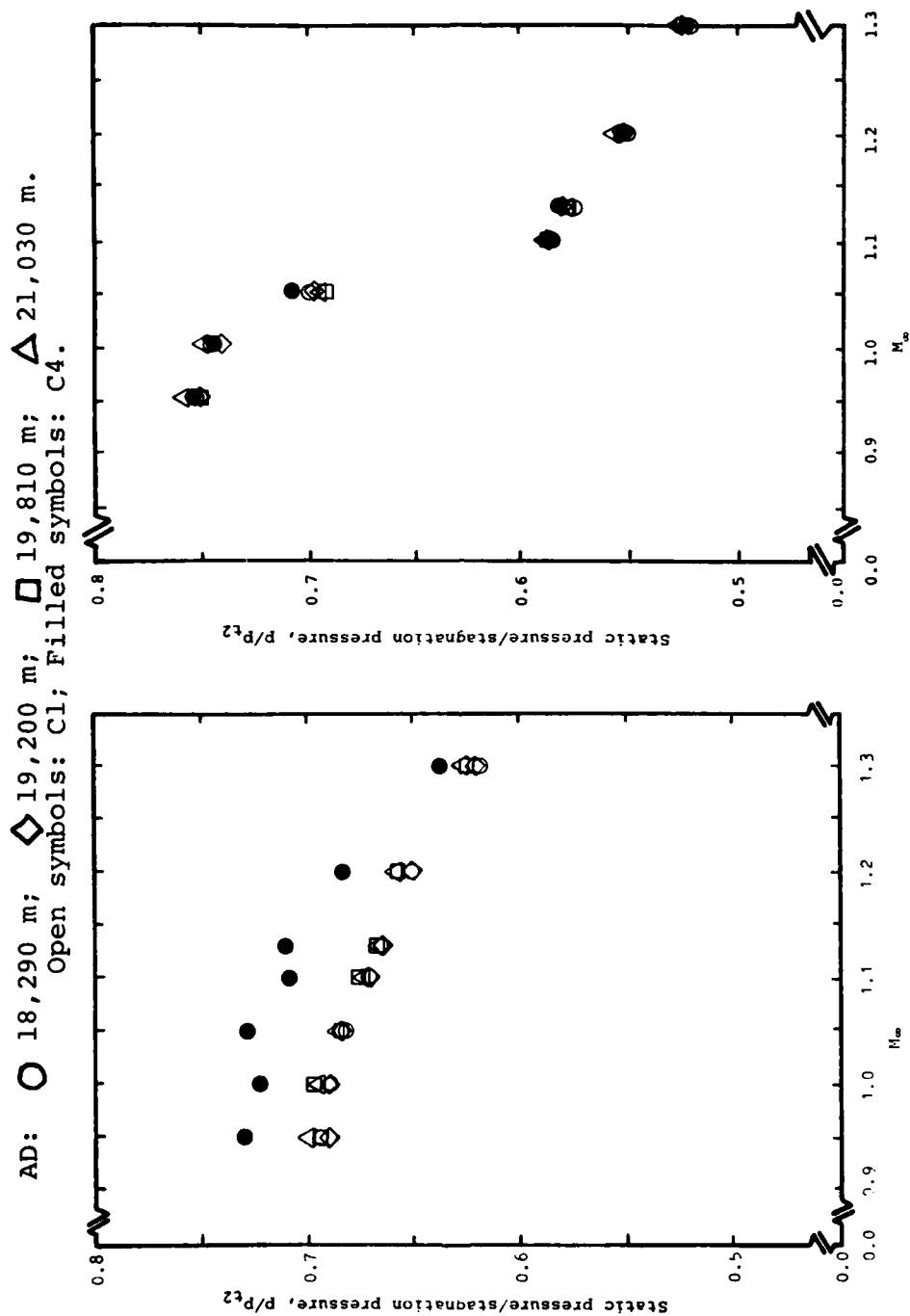


Figure 14. Concluded: (c) $x = 0.551 x_0$ (tap 18), and (d) $x = 1.000 x_0$ (tap 22).

Rewriting this expression in terms of the pressure ratio used in figure 14, we obtain

$$\frac{p}{p_{t2}} = \frac{p_{\infty}}{p_{t2}} \frac{0.7C_1 M_{\infty}^2}{\sqrt{M_{\infty}^2 - 1}} + 1 \quad (4)$$

Using the Ames tables⁵ to obtain the value of p_{∞}/p_{t2} as a function of Mach number, one finds the following values:

$$\begin{aligned} \frac{p}{p_{t2}} &= 0.5595 [0.7C_1 (2.8903) + 1] \text{ for } M_{\infty} = 0.95 \\ &= 0.4689 [0.7C_1 (2.6402) + 1] \text{ for } M_{\infty} = 1.10 \\ &= 0.3685 [0.7C_1 (2.0345) + 1] \text{ for } M_{\infty} = 1.30 \end{aligned}$$

Using this relatively simple approximation, one would expect the pressure ratio p/p_{t2} to decrease with Mach number for these test conditions. Thus, although one would predict a greater decrease in the pressure ratio using equation (4) than is actually exhibited by the data, the small-deflection approximation provides a qualitative substantiation of the observed Mach-number dependence.

Although the pressures measured on the conical surface exhibit an inverse dependence on M_{∞} , the pressure ratio (p/p_{t2}) for locations on the blunt face would be independent of the Mach number for supersonic flows. The data from the orifice on the flat face (see the pressure measurements for $x = 0.0$, presented in figures 12 and 13) exhibit this Mach-number independence.

As noted when figures 11 through 13 were discussed, the pressure ratio at $x = 1.000 x_0$ exhibits a much greater variation with Mach number than occurred at the other orifices. As can be seen in the measurements presented in figure 14d, the Mach-number dependence apparently reflects a change in the downstream flow field that occurs in the transonic speed range. These transonic changes in the flow field occur far enough downstream (on the second conical segment) that they do not affect the flow through the fluidic generator.

⁵ Ames Research Staff, *Equations, Tables, and Charts for Compressible Flow*, Report 1135, 1953, National Advisory Committee for Aeronautics (NACA).

3.2 Flow Through Fluidic Generator and Internal Pressure Measurements for 0° Angle of Attack

As has been discussed, the air which activates the fluidic generator enters the inlet hole in the stagnation region, passes through the resonator-interaction region of the generator assembly and then into the internal chamber, before it finally flows through the exhaust ports. A sketch of this internal flow pattern and of the relevant pressure instrumentation is presented in figure 15. The mass-flow rate through the fluidic generator was calculated with the pressures measured at the orifices of figure 15, using three different assumptions regarding the air flow through the fluidic generator.

Flow Model 1.--Because the area of the annular gap around the nozzle centerbody is so much less than the area of the inlet hole, it is assumed that the air velocity forward of the centerbody is relatively small. Thus, as indicated in figure 15, this region serves as a reservoir (or stagnation chamber) for the nozzle centerbody. This element of the assumed flow model is supported by the static-pressure measurements from this region that are presented in figure 16. The static pressures both at tap 25 ($x = 0.026 x_0$) and at tap 26 ($x = 0.132 x_0$) are essentially equal to p_{t2} over the entire range of Mach number and of density altitude for the conditions of the present test program.

It is assumed that the flow accelerates isentropically from this "reservoir" through the annular gap, reaching the speed of sound at the minimum cross-sectional area of the annular gap. Thus, the centerbody serves as a throat, "choking" the flow over the entire range of test conditions for this program. Fliegner's formula⁷ for the choked flow of perfect air along with the minimal cross-sectional area, A_{In} , can be used to calculate the mass-flow rate, \dot{m}_1 :

$$\frac{\dot{m}_1}{\rho_\infty U_\infty A_{In}} = \frac{0.0386 [p(25)]}{\rho_\infty U_\infty \sqrt{T_t}}, \quad (5)$$

⁷ A. H. Shapiro, The Dynamics and Thermodynamics of Compressible Fluid Flow, Ronald Press, New York, 1953.

①, ②, ③ Assumed flow models,
described in text

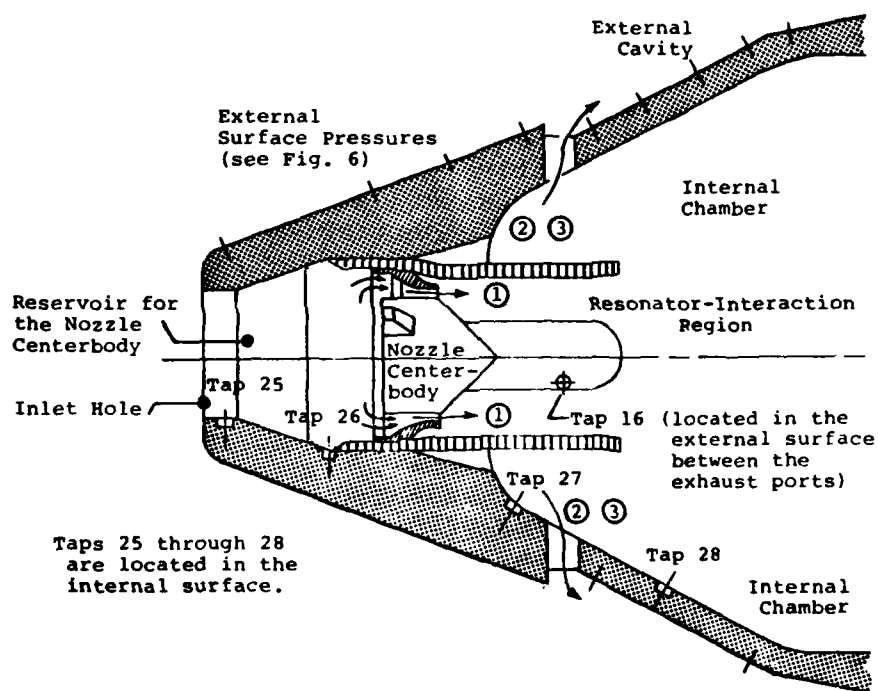


Figure 15. Internal flow pattern and relevant pressure information.

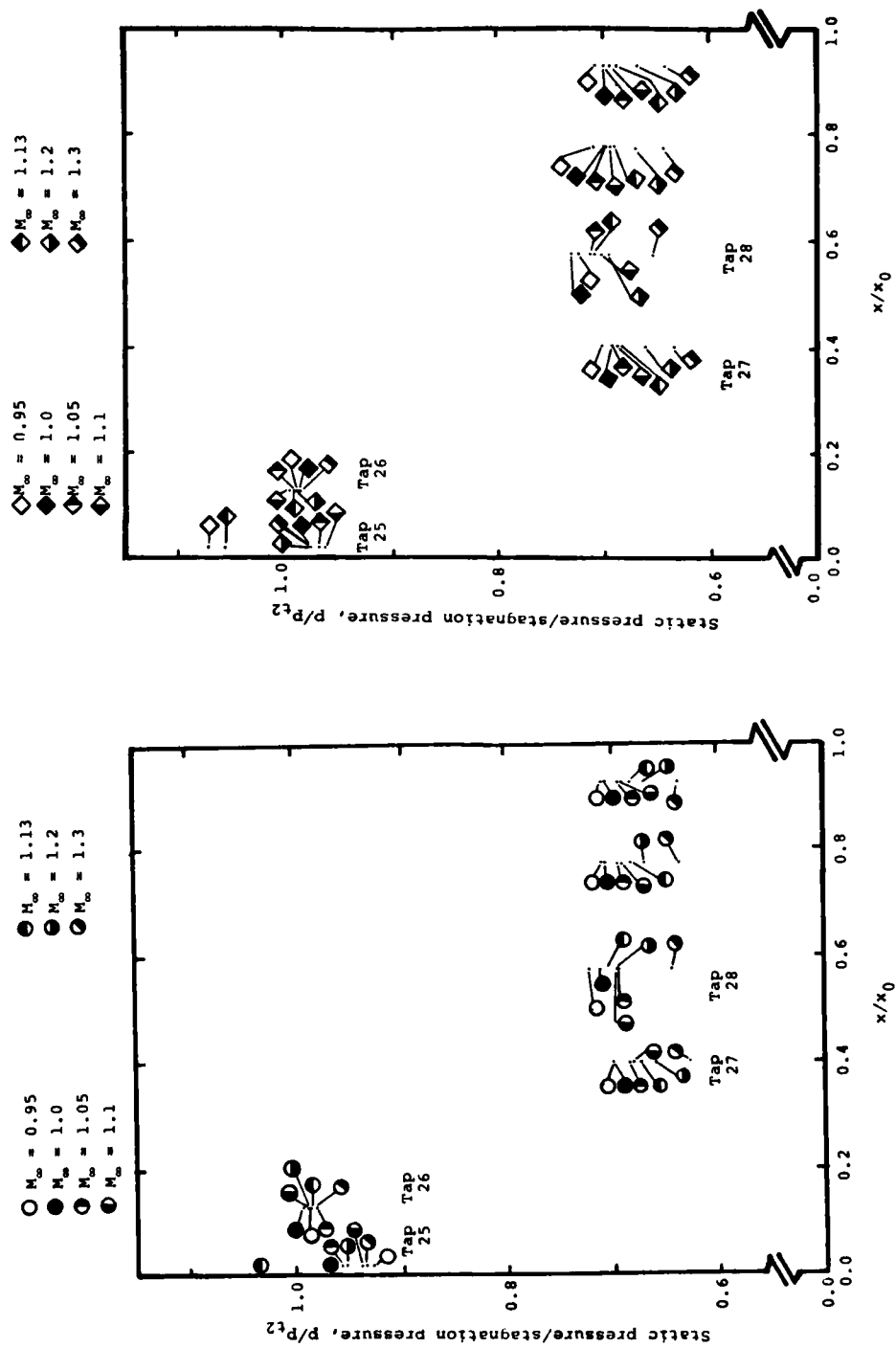


Figure 16. Static pressure distributions on internal surface of C1:
(a) $AD = 18,290$ m; and (b) $AD = 19,200$ m.

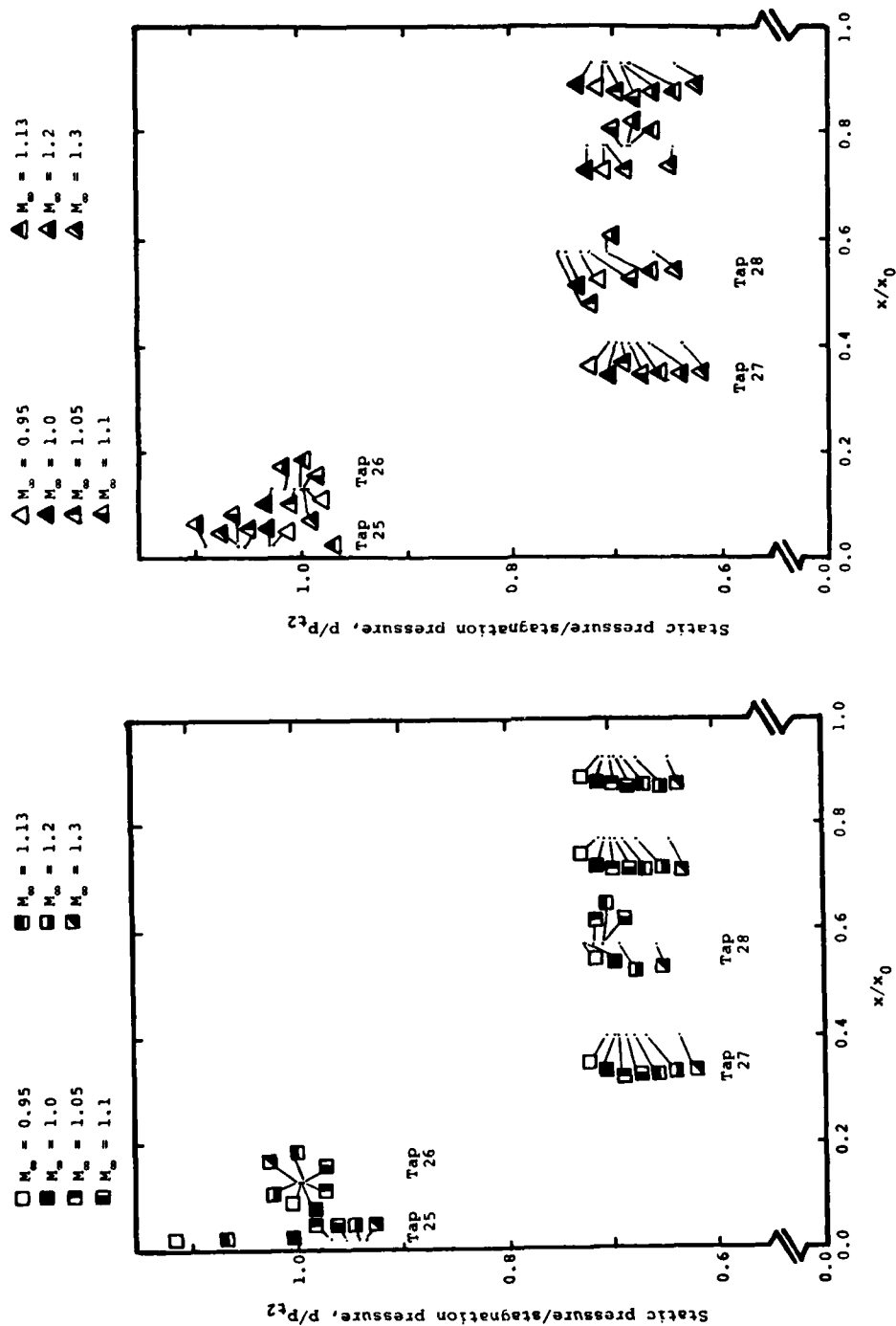


Figure 16. Concluded: (c) AD = 19,810 m; and (d) AD = 21,030 m.

where ρ_∞ = free-stream density (kg/m^3), U_∞ = free-stream velocity (m/s), and T_t = stagnation temperature (K). The local mass-flow rate has been divided by $\rho_\infty U_\infty A_{In}$ (which is equal to the free-stream mass-flow rate across an area equal to that of the inlet hole) in order to obtain a dimensionless parameter. As will be seen, dividing the local mass-flow rates by $\rho_\infty U_\infty A_{In}$ yields a dimensionless parameter which is independent of the Mach number and of the density altitude over the range of test conditions. This is true for the mass-flow rates for all the assumed flow models.

Because the air must go around the corner of a flat-faced cylinder as it enters the nozzle centerbody (producing a separation bubble) and because of the presence of boundary layers on both surfaces of a narrow annular gap, it is expected that the effective throat area is significantly less than the minimum cross section of the annular gap (which is the area used in eq. (5)). Thus, it is expected that the nondimensionalized values of \dot{m}_1 , as calculated using equation (5) (which are represented by the half-filled symbols of fig. 17), overestimate the actual mass-flow rate.

It is believed that the flow is indeed choked by the nozzle centerbody, even though the static pressures in the (downstream) internal chamber are approximately $0.7 p_{t2}$. The reason for the chamber value of $0.7 p_{t2}$ follows. The pressure in the internal chamber is governed (1) by the pressure in the external cavity (which is established by the external flow field), since (as will be discussed) the flow through the exhaust ports is not choked, and (2) by the pressure drop across the exhaust ports, which is governed by the mass-flow rate, as shown in equation (7a). The mass-flow rate is established by the choking of the flow through the nozzle centerbody. The static pressure increases from the sonic value ($0.53 p_{t2}$) at the throat of the nozzle centerbody to $0.7 p_{t2}$, the value in the internal chamber, as it flows through the resonator-interaction region of the generator assembly (see figs. 1b and 15) and into the internal chamber.

Flow Model 2.--The mass-flow rate for the second flow model was calculated assuming that the flow through the exhaust ports is choked. Thus, for the flow model, it is assumed that the static pressure in the external cavity in the region of the exhaust ports--i.e., $[p(16)]$ --is approximately half, or less, of the pressure in the internal chamber--i.e., $[p(27)]$ or $[p(28)]$. Assuming that the flow through the exhaust ports is choked, Fliegner's formula can be used to calculate the total mass-flow rate through the 24 exhaust ports:

AD: ○ 18,290 m; ◇ 19,200 m; □ 19,810 m; △ 21,030 m.
 Half-filled symbols: $m_i = \dot{m}_1$; Filled symbols: $m_i = \dot{m}_2$;
 Open symbols: $m_i = \dot{m}_3$.

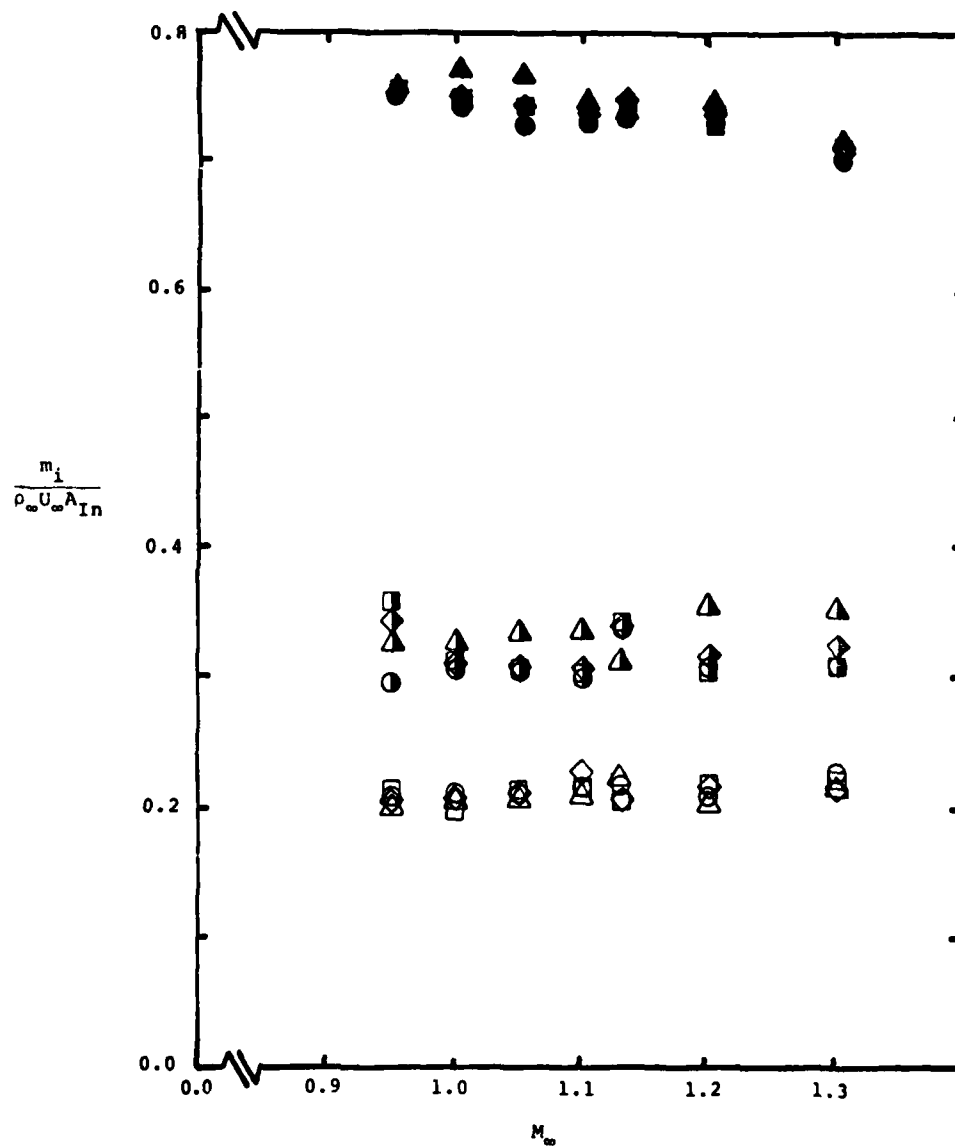


Figure 17. Mass-flow rate through fluidic generator of C1
 (as calculated for various assumptions).

$$\frac{\dot{m}_2}{\rho_\infty U_\infty A_{In}} = \frac{0.0638[p(27) + p(28)]}{\rho_\infty U_\infty \sqrt{T_t}} \quad (6)$$

The mass-flow rate (\dot{m}_2) thus calculated is represented by the filled symbols of figure 17. The mass-flow rates calculated using this flow model are much higher than those calculated using the other two flow models. This flow model overestimates the mass-flow rate because the flow is not choked at the exhaust ports. The conclusion that the flow is not choked at the exhaust ports is verified by the pressure ratio across them. As shown in the data of figure 18, the pressure drop across the exhaust ports is less than 10 percent.

The conclusion that the flow is choked not at the exhaust ports but at the nozzle centerbody for C1 over the range of test conditions is very important. It has been shown that the pressure ratio (p/p_{t2}) for the separated region of the external cavity is a well-behaved function of the free-stream Mach number and is independent of density altitude (as shown in figs. 8 through 14). Since the pressure drop across the exhaust ports is relatively small and is a function of the mass-flow rate through the fluidic generator, the pressure in the internal chamber (which is the "back pressure" for the resonator-interaction region of the fluidic generator) follows the external pressure. However, since the flow is choked by the nozzle centerbody, the inlet pressure for the resonator-interaction region is a fixed fraction of p_{t2} (i.e., 0.53, the sonic value). It is expected that the details of the flow field in the resonator depend on the pressure differences across it.

Flow Model 3.--For the third flow model, the volumetric flow-rate, Q , was calculated using the equation for subsonic flow through a sharp-edged, circular orifice⁸:

$$Q = 0.6YA \sqrt{\frac{2\Delta p}{\rho}} \quad (7a)$$

For the orifice ratios and for the Reynolds numbers of the present tests,

⁸ *Flow of Fluids Through Valves, Fittings, and Pipes, Technical Paper No. 410, The Crane Company.*

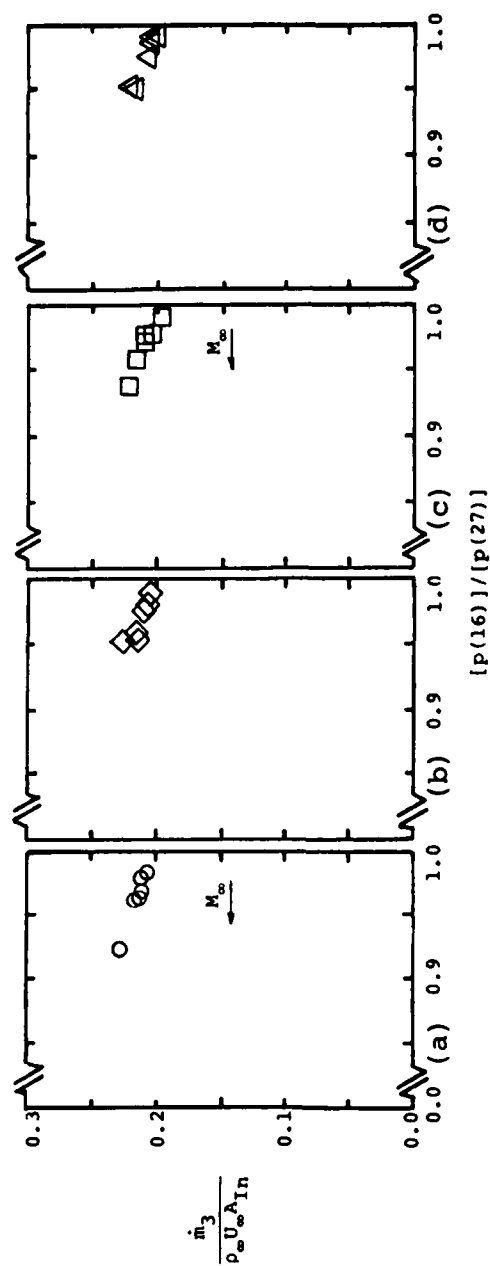


Figure 18. Mass-flow rate as calculated for flow-model 3 as a function of pressure drop across exhaust ports: (a) AD = 18,290 m; (b) AD = 19,200 m; (c) AD = 19,810 m; and (d) AD = 21,030 m.

$$Y = \left\{ 1.0 - 0.3 \frac{\Delta p}{P_1} \right\}. \quad (7b)$$

Furthermore, it is assumed that the acceleration of the flow from the internal chamber through the exhaust ports is such that

$$\rho \propto p. \quad (7c)$$

Combining these relations, one can calculate the mass-flow rate for this model using the relation

$$\frac{\dot{m}_3}{\rho_\infty U_\infty A_{In}} = \frac{0.158 p(16)}{\rho_\infty U_\infty \sqrt{T_t}} \left\{ 0.7 + 0.3 \frac{p(16)}{p(27)} \right\} \sqrt{1.0 - \frac{p(16)}{p(27)}}. \quad (8)$$

The mass-flow rates thus calculated are presented as a function of M_∞ in figure 17 (as the open symbols) and as a function of the pressure drop across the exhaust ports in figure 18. As has been discussed, the pressure drop across the exhaust ports (the pressure ratio $[p(16)]/[p(27)]$) for these flow conditions is relatively small. The nondimensionalized mass-flow rate increases slightly as the pressure ratio decreases. As indicated by the arrow, the pressure drop across the exhaust ports decreases as the Mach number increases. The correlation between the pressure drop and the dimensionless mass-flow rate is the same for all four density altitudes.

The experimentally determined values of the pressure ratio $[p(16)]/[p(27)]$ indicate that the flow in this region is incompressible. Thus, the assumptions made in developing flow model 3 are quite realistic. Since the two pressures needed to calculate the flow field were measured directly, it is believed that the mass-flow rates calculated using equation (8), i.e., \dot{m}_3 , are the most realistic of those presented in figure 17.

3.3 External and Internal Flow-Fields for C2 at 0° Angle of Attack

As shown in figure 1c, an ogive angle adapter was placed over the first conical segment of the standard nose cone to form C2. The presence of the adapter served to increase the deflection angle of the first conical segment to

35°17' and to increase the effective height of the separation step for the external cavity. The increased deflection angle should affect the external flow field for these transonic flows. Increasing the height of the separation step caused the streamwise extent of the separated region to increase and the static pressure in the separated region to decrease. The static-pressure distribution for the external surface of C2 is presented in figure 19. The static pressures in the external cavity of C2 are much less than those for C1. Furthermore, whereas the pressure ratio (p/p_{t2}) at a given location (tap) for C1 decreases slowly as M_∞ increases (e.g., see fig. 14c), the pressure ratio for C2 decreases much more rapidly with M_∞ .

Internal pressure distributions for C2 are presented in figure 20. These pressure measurements were obtained at a simulated density altitude of 18,290 m over the entire Mach-number range of the present tests. At the lowest free-stream Mach number (0.95), the pressure drop across the exhaust ports is relatively small. At $x = 0.443 x_0$ (the location of tap 16, between the exhaust ports), the pressure in the external cavity is approximately 0.45 p_{t2} (see fig. 19), whereas the pressure in the internal chamber is approximately 0.55 p_{t2} (see fig. 20). Thus, as was true for the entire range of test conditions for C1, the flow through the exhaust ports is incompressible, and subsonic when $M_\infty = 0.95$ for C2. However, for $M_\infty = 1.3$, the pressure in the external cavity between the exhaust ports is approximately 0.21 p_{t2} , whereas it is 0.38 p_{t2} in the internal chamber. This pressure ratio is only slightly greater than the value for the onset of sonic (or choked) flow through the exhaust ports. Thus, when $M_\infty = 1.3$, the separation of the flow from the forward conical segment of C2 causes the pressure in the external cavity to decrease toward the condition where the exhaust ports (and not the minimum area of the nozzle centerbody) would become dominant in determining the mass-flow rate through the generator assembly. However, even at the highest Mach number of the present tests (1.3), the condition of sonic flow through the exhaust ports is not reached. Therefore, even though the relatively large separation-step height of C2 causes the external cavity pressure to be relatively low, the mass-flow rates through the generator assembly are such that the pressure in the internal chamber can decrease also. Thus, over the entire Mach-number range, the nozzle centerbody is the dominant constriction and the flow through the exhaust ports is subsonic.

C1: $\circ M_\infty = 0.95$; $\diamond M_\infty = 1.1$; $\triangle M_\infty = 1.3$
C2: $\circ M_\infty = 0.95$; $\diamond M_\infty = 1.1$; $\triangle M_\infty = 1.3$

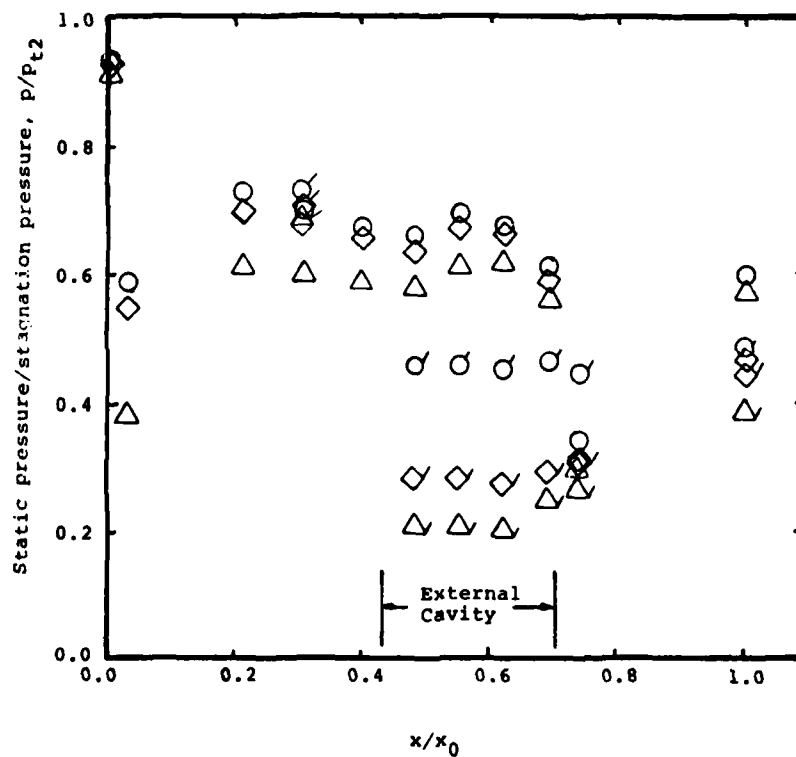


Figure 19. Comparison of external pressure distributions for C1 and C2; AD = 18,290 m.

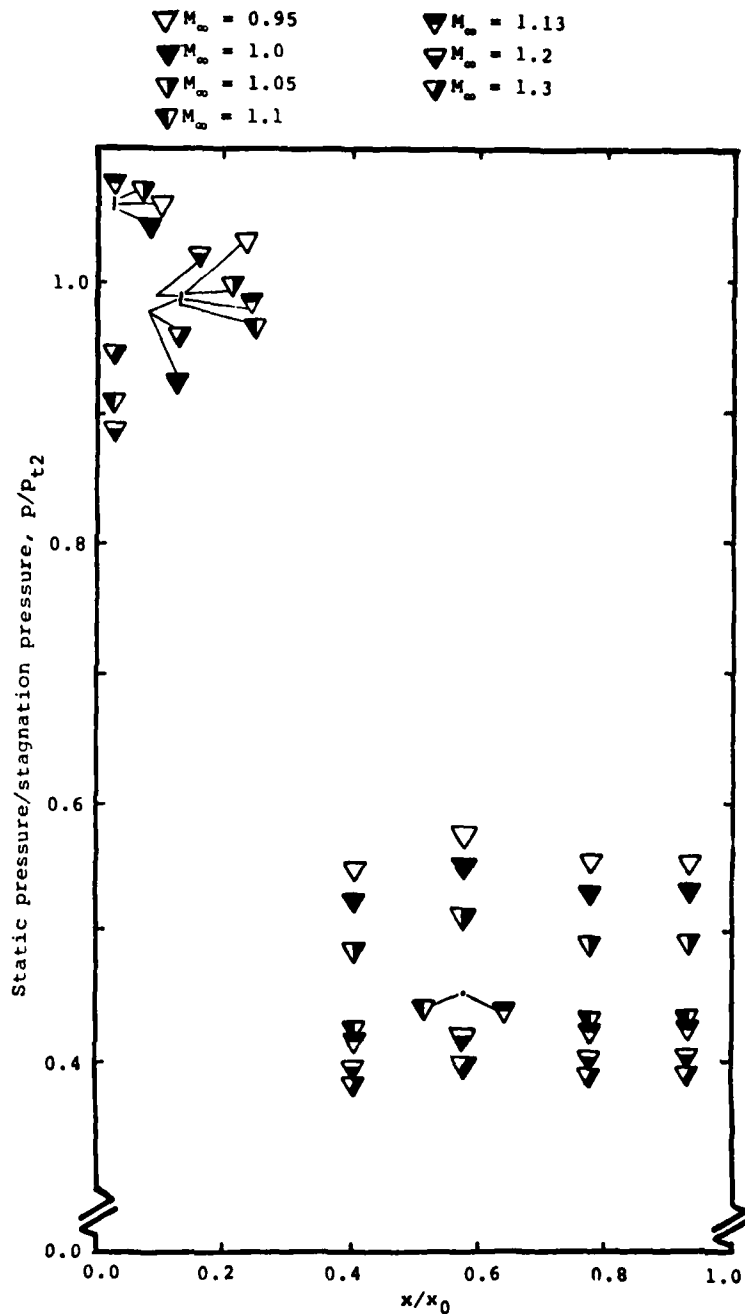


Figure 20. Internal pressure distribution for C2; AD = 18,290 m.

This conclusion is supported by the calculated mass-flow rates presented in figure 21. For $M_\infty = 1.13$, the mass-flow rates as calculated using either equation (5) or equation (8) are essentially the same for C1 and for C2. The agreement between the \dot{m}_1 calculations for these conditions should be expected, since the flow is choked by the nozzle centerbody, and since the values of p_{t2} and the geometries both of the inlet hole and of the nozzle centerbody are the same for C1 and C2. The good agreement between the \dot{m}_3 calculations (even though the assumption that the flow is incompressible breaks down for C2 but remains true for C1 as M_∞ increases) is attributed to the fact that the two pressures required for equation (8) are measured directly.

The difference in pressure between the value at the throat of the nozzle centerbody (where the flow is sonic) and that in the internal chamber (as indicated by the data of fig. 20) varies more with the test conditions for C2 than it did for C1. Thus, significant changes in the flow field for the resonator-interaction region are expected.

3.4 The Effect of Angle of Attack

Data were obtained over an angle-of-attack range from 0° to 10° . The effect of the angle of attack, α , on the flow field for C1 is indicated by the data presented in figures 22 and 23. The pressure distributions for the external surface are presented in figure 22 for $\alpha = 5^\circ$. The pressures on the leeward side ($PHIT = 0^\circ$) are within 10 percent of the windward values.

The mass-flow rates are presented as a function of the Mach number for simulated density altitudes from 18,290 m to 21,030 m for $\alpha = 0^\circ$ and for 18,290 m for $\alpha = 5^\circ$. Only one test condition is represented for $\alpha = 10^\circ$: $M_\infty = 1.1$ and $AD = 18,290$ m. Only values calculated using equation (8) (that is, \dot{m}_3) are presented in figure 23, since these were believed to be the most accurate calculations.

The angle of attack had relatively little effect on the surface pressures or on the mass-flow rates over the range of α considered in the present program.

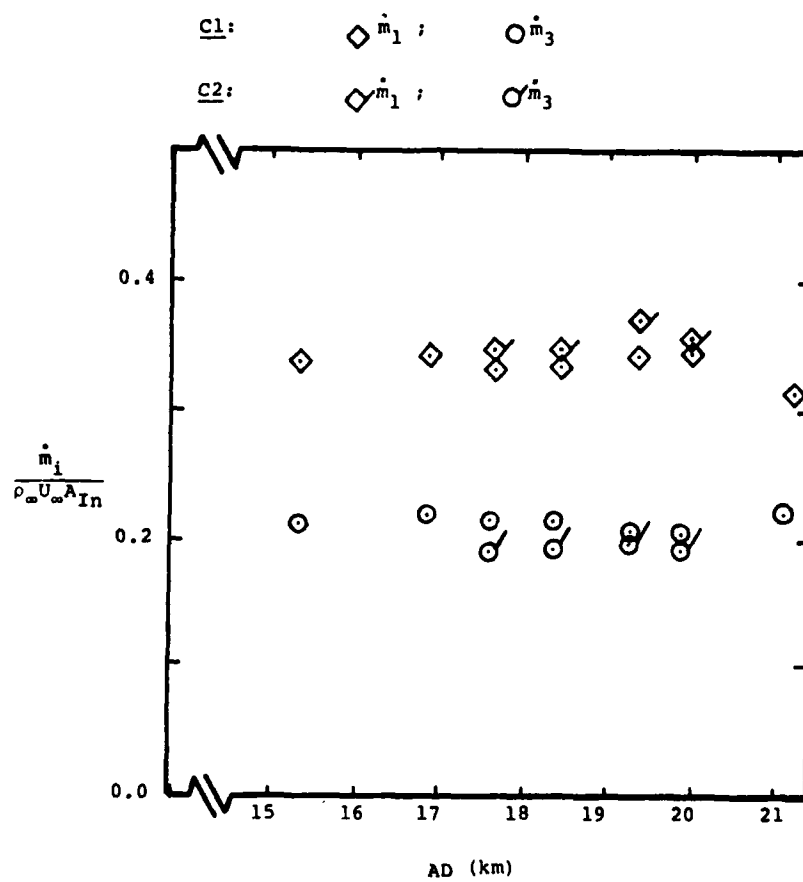


Figure 21. Comparison of mass-flow rates for C1 and C2; $M_\infty = 1.13$.

$\circ M_\infty = 0.95$; $\diamond M_\infty = 1.0$; $\triangle M_\infty = 1.05$; $\square M_\infty = 1.1$; $\bigcirc M_\infty = 1.2$; $\nabla M_\infty = 1.3$

Flagged PHIT = 180° ; Unflagged PHIT = 0°

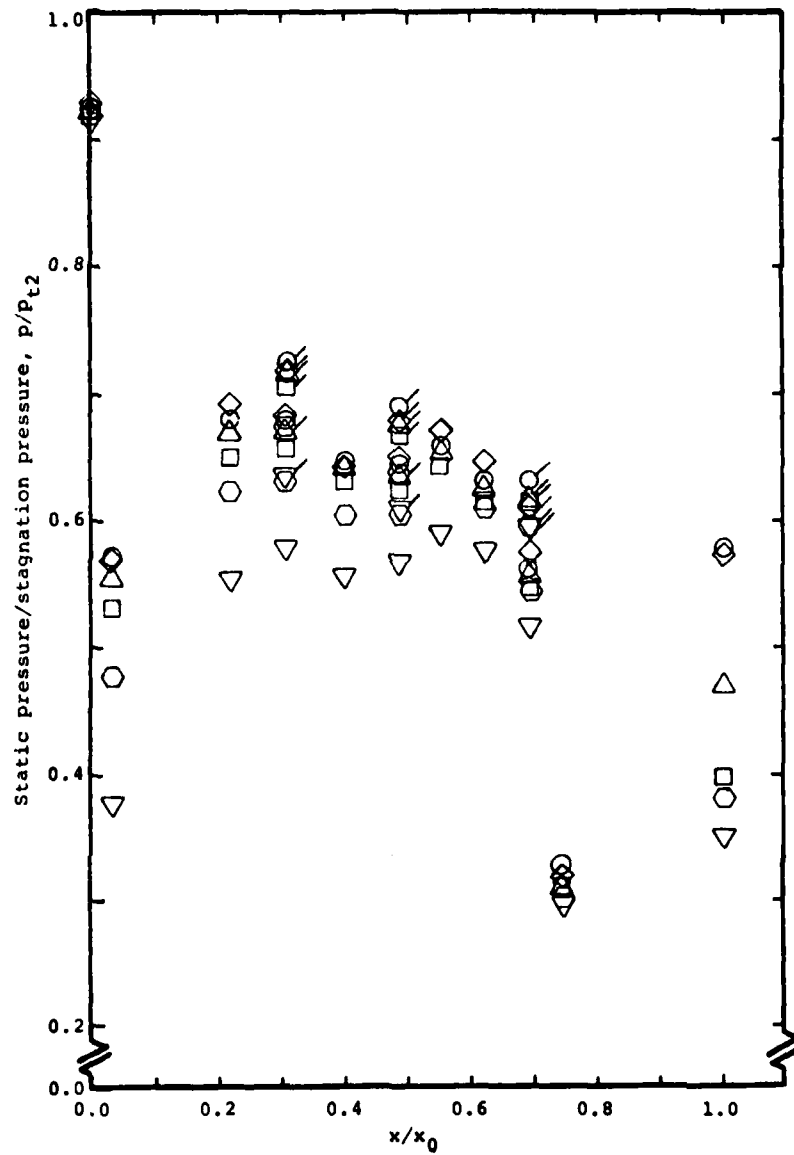


Figure 22. External pressure distribution for C1 at $\alpha = 5^\circ$; AD = 19,200 m.

$\alpha = 0^\circ$: \circ AD = 18,290 m; \diamond 19,200 m; \square 19,810 m; \triangle 21,030 m.
 $\alpha = 5^\circ$: \bullet AD = 18,290 m;
 $\alpha = 10^\circ$: \bullet AD = 18,290 m;

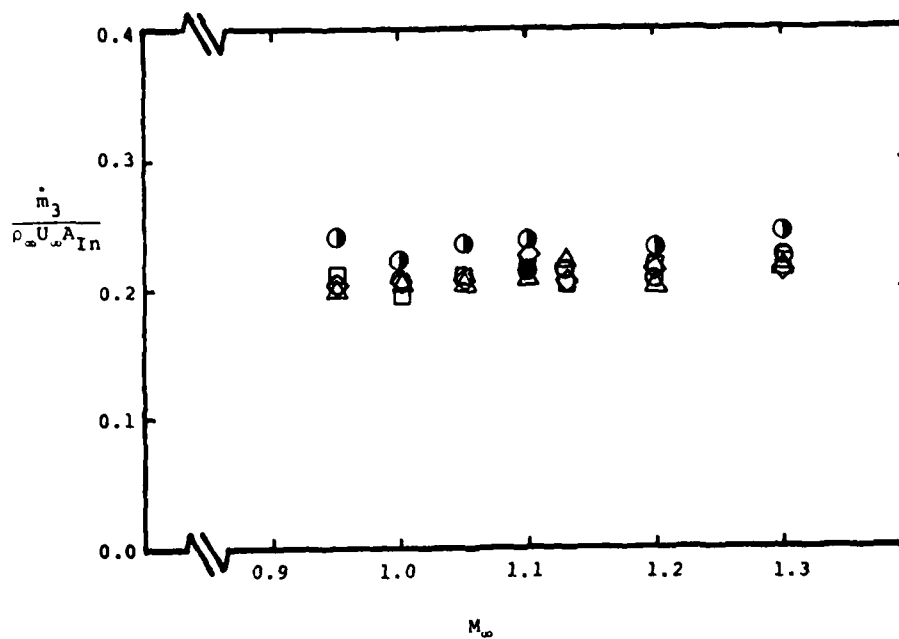


Figure 23. Effect of angle of attack on mass-flow rate for Cl.

4. CONCLUSIONS ABOUT FLOW FIELD

An experimental program has been conducted to evaluate the performance of the fluidic-generator/fuze assembly of the Army MLRS in the transonic speed range. The test program, which was conducted in the Aerodynamics Wind Tunnel at AEDC, used full-scale models of the standard nose cones. The test conditions included free-stream Mach numbers from 0.95 to 1.3 over a range of free-stream densities simulating altitudes from 15,240 m to 21,030 m. Over the range of test conditions covered in the present program, the following conclusions are made. Neither the angle of attack nor the simulated density altitude (or, equivalently, the Reynolds number) had a significant effect on the flow field. Thus, reference is not made to these parameters in the discussion that follows. Although the configuration of primary interest to this program was C1, the conclusions are valid both for C1 and for C2, unless specifically stated otherwise.

4.1 External Flow Field

Shock-layer flow for flat face.--The pressure distribution across the flat face of the nose cone (region 1 in fig. 24) is similar to that presented in figure 3, decreasing gradually in the radial direction from p_{t2} (the stagnation pressure downstream of a normal shock wave) at the axis of symmetry until the corner is reached. Thus, the air which enters the inlet hole has passed through the normal (or nearly normal) portion of the shock wave. The pressure measurements from this region (especially those measured using the Pitot probes) were closely predicted using the relatively simple analysis of section 3.1.1.

Flow over the ogive.--At all the orifices from $x = 0.030 x_0$ to $x = 1.000 x_0$, the ratio p/p_{t2} at a particular orifice decreased as the Mach number increased. Furthermore, the Mach number variations are gradual and consistent for C1, except for the two extreme orifices: the one at $x = 0.030 x_0$ (where the pressure is apparently affected by a separation bubble at the corner) and the one at $x = 1.000 x_0$ (where the pressure reflects changes in the transonic flow field). A similar Mach-number dependence in the pressure measurements occurs both for orifices on the forward conical surface and for those in the external cavity for C1. Since the data exhibit a consistent Mach-dependence that is qualitatively supported by the small deflection approximation (i.e., eqs. (2) through (4)), a relatively simple empirical correlation (based on the data of figs. 11 through 14) could

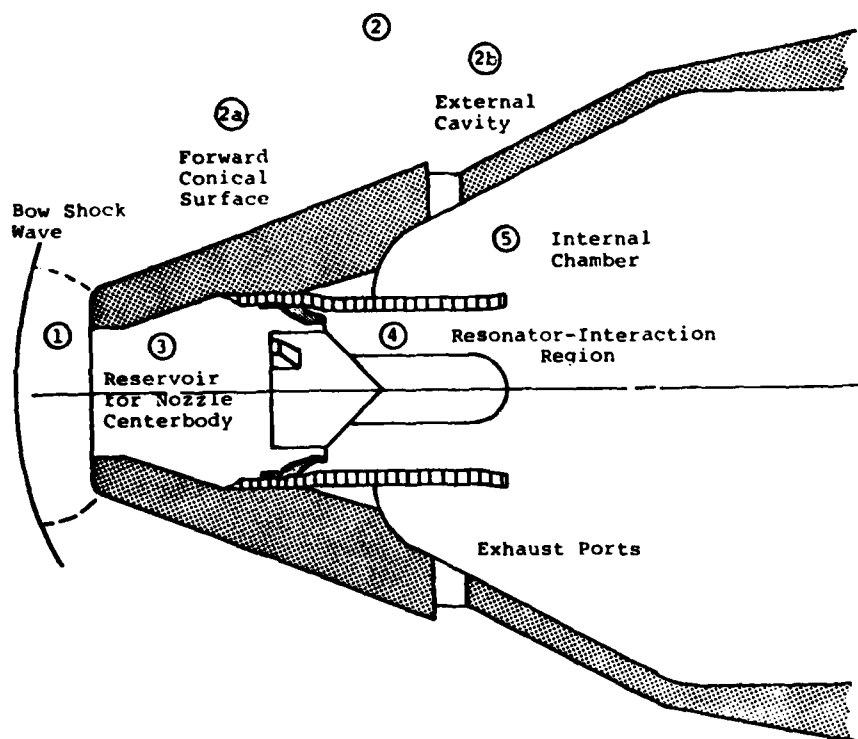


Figure 24. Flow field.

be developed to predict the pressure ratio at a given location for a given flow condition. This is most important, since the pressure at $x = 0.443 x_0$ in the external cavity is back pressure for the flow through the exhaust ports.

Because of the relatively large separation step for C2, the pressures in the external cavity were much more sensitive to the free-stream Mach number. Thus, a more detailed analysis would be needed for this configuration.

4.2 Internal Flow Field

Reservoir for the nozzle centerbody.--Since the cross section of the annular area around the nozzle centerbody (region 3 of fig. 24) is so much smaller than that of the inlet hole and of the reservoir, this region serves as a stagnation chamber (or reservoir) for the flow through the annular gap. Thus, the pressure in this region is p/p_{t2} , which can be readily calculated for given free-stream conditions. For all the test conditions considered, the mass-flow rate of air through the generator assembly was limited (choked) by the nozzle centerbody. However, because of the blunt, sharp-edged geometry of the upstream face of the centerbody and because of the viscous boundary layers on the walls of the annulus, the mass-flow rates calculated using Fliegner's formula (eq. (5)) for this "throat" were not good approximations of the actual flow rate.

Flow in the resonator-interaction region.--Measurements that could provide information about the details of the flow through the resonator-interaction region (region 4 of fig. 24) were not made. However, because the flow is choked by the nozzle centerbody, the inlet pressure is approximately $0.53 p_{t2}$. The back pressure for the resonator-interaction region is the pressure in the internal chamber, which varies with configuration and with flow condition.

Flow in the internal chamber.--Flow is subsonic as it passes through the exhaust ports. Thus, the pressure in the internal chamber (region 5 of fig. 24) is governed (1) by the pressure in the external cavity (which is established by the external flow field), since the flow through the exhaust ports is not choked, and (2) by the pressure drop across the exhaust ports, governed by the mass-flow rate (which is fixed by the choking of the flow through the nozzle centerbody). The mass-flow rate of air through the nozzle generator seems to be best predicted by equation (8).

4.3 Final Comments

When establishing an experiment simulating conditions similar to the geometries and the flow conditions of the present tests, the two most important pressures are (1) that at the inlet hole (region 1), and (2) that in the separated region of the external cavity where the exhaust ports are located (region 2b). Over the range of test conditions considered, suitable correlations for these two pressures have been exhibited by the data for C1.

NOMENCLATURE

| | |
|------------|--|
| A | cross-sectional area |
| A_{In} | cross-sectional area of the inlet hole |
| AD | altitude simulated by free-stream density |
| C_p | pressure coefficient |
| m_i | mass-flow rate for flow model i , where i is 1, 2, or 3 |
| M_∞ | free-stream Mach number |
| p | static pressure (N/m^2) |
| p(16) | static pressure in the external cavity between the exhaust ports (N/m^2) (see fig. 15 and eq. (8)) |
| p(25) | static pressure at the inlet hole (N/m^2) (see fig. 15 and eq. (5)) |
| p(27) | static pressure in the internal chamber (N/m^2) (see fig. 15 and eqs. (6) and (8)) |
| p(28) | static pressure in the internal chamber (N/m^2) (see fig. 15 and eq. (6)) |
| P_{t2} | stagnation pressure downstream of a normal shock wave |
| P_∞ | free-stream static pressure |
| PHIT | angular location of the pressure taps ($^\circ$), (see fig. 1a) |
| Q | volumetric-flow rate (see eq. (7a)) |
| r | radial coordinate (see fig. 3) |
| R_{ff} | radius of flat face (see fig. 3) |

| | |
|---------------|--|
| T_t | stagnation temperature (K) |
| U_∞ | free-stream velocity (m/s) |
| x | longitudinal distance from the model nose (cm) |
| x_0 | reference length (7.696 cm) |
| Y | factor defined in equation (7b) |
| α | angle of attack |
| γ | ratio of specific heats |
| ρ_∞ | free-stream density (kg/m^3) |

LITERATURE CITED

1. J. E. Fine, Preliminary Analysis of Pressure Measurements in MLRS Nov. 80 Wind Tunnel Test, DELHD-DE-OP, Jan. 81, HDL Office Memo.
2. D. A. Hodges, Performance Evaluation of the XM-445 Fluidic Generator Fuze Assembly at Mach Numbers from 0.95 to 1.3, AEDC-TSR-80-P81, Dec. 1980, AEDC.
3. R. L. Goodyear and H. Lee, Performance of the Fluidic Power Supply for the XM-445 Fuze in Supersonic Wind Tunnels, HDL-TM-81-4, Feb. 1981, Harry Diamond Laboratories.
4. J. C. Boison and H. A. Curtiss, An Experimental Investigation of Blunt Body Stagnation Point Velocity Gradient, ARS Journal, Feb. 1959, Vol. 29, No. 2, pp. 130-135.
5. Ames Research Staff, Equations, Tables, and Charts for Compressible Flow, Report 1135, 1953, NACA.
6. F. G. Moore and R. C. Swanson, Jr. Aerodynamics of Tactical Weapons to Mach Number 3 and Angle of Attack 15°, Part I--Theory and Application, NSWC/DL TR-3584, Feb. 1977, Naval Surface Weapons Center.
7. A. H. Shapiro, The Dynamics and Thermodynamics of Compressible Fluid Flow, Ronald Press, New York, 1953.
8. Flow of Fluid Through Valves, Fittings, and Pipes, Technical Paper No. 410, The Crane Company.

BLANK DELIBERATELY

DISTRIBUTION

ADMINISTRATOR
DEFENSE TECHNICAL INFORMATION CENTER
ATTN DTIC-DDA (12 COPIES)
CAMERON STATION, BUILDING 5
ALEXANDRIA, VA 22314

HARRY DIAMOND LABORATORIES
ATTN CO/TD/TSO/DIVISION DIRECTORS
ATTN RECORD COPY, 81200
ATTN HDL LIBRARY, 81100 (3 COPIES)
ATTN HDL LIBRARY, 81100 (WOODBIDGE)
ATTN TECHNICAL REPORTS BRANCH, 81300
ATTN CHAIRMAN, EDITORIAL COMMITTEE
ATTN LEGAL OFFICE, 97000
ATTN CHIEF, 20240
ATTN CHIEF, 34400
ATTN CHIEF, 34600 (4 COPIES)
ATTN FINE, J., 34600 (2 COPIES)
ATTN DEADWYLER, R., 13400

COMMANDER
US ARMY MISSILE COMMAND
ATTN DRCPM-RS, MLRS
(CROSSWHITE, B.) (10 COPIES)
REDSTONE ARSENAL, AL 35809

COMMANDANT
US ARMY WAR COLLEGE
ATTN LIBRARY
CARLISLE BARRACKS, PA 17013

SUPERINDENT
HQ, USMA
ATTN TECHNICAL LIBRARY
WEST POINT, NY 10996

